Journal of Fluids and Structures 128 (2024) 104137

Contents lists available at ScienceDirect

Journal of Fluids and Structures

journal homepage: www.elsevier.com/locate/jfs

Effect of aspect ratio on flow-induced vibration of oblate spheroids and implications for energy generation

Adrian Cordero Obando [a,*], Mark C. Thompson [a], Kerry Hourigan [a], Jisheng Zhao [a,b]

[a] *Fluid Laboratory for Aeronautical and Industrial Research (FLAIR), Monash University, Clayton, Victoria 3800, Australia*
[b] *School of Engineering and Technology, University of New South Wales, Canberra, ACT 2600, Australia*

ARTICLE INFO

Keywords:
Flow-induced vibration
Flow-induced vibration energy harvesting
Bluff bodies
Spheroids
Oblate spheroids

ABSTRACT

This study experimentally investigates the influence of aspect ratio on cross-flow flow-induced vibration (FIV) of elastically mounted oblate spheroids. The aspect ratio ($\epsilon = b/a$) of an oblate spheroid, defined as the ratio of the major diameter (b) in the cross-flow direction to the minor diameter (a) in the streamwise direction, was varied between 1.00 and 3.20. The FIV response was characterized over a range of reduced velocity, $3.0 \leqslant U^* = U/(f_{nw}b) \leqslant 12.0$, where U is the free-stream velocity and f_{nw} is the natural frequency of the system in quiescent water. The corresponding Reynolds number varied over the range $4730 \leqslant Re \leqslant 20\,120$. It was found that in addition to the vortex-induced vibration (VIV) Mode I and Mode II responses observed for a sphere, on increasing the aspect ratio to $\epsilon = 1.53$ and 2.0, a galloping-dominated response, denoted by G-I, was encountered at high reduced velocities. With a further increase in aspect ratio to $\epsilon = 2.50$, the body vibration exhibited an additional VIV-like response (V-I) following the sequential appearance of Mode I, Mode II and G-I, with smooth transitions between these modes. In the case of the largest aspect ratio considered in the present study, $\epsilon = 3.20$, the spheroid intriguingly exhibited only a pure VIV Mode I before transitioning to a VIV-dominated mode, namely V-II. The largest vibration amplitude observed was $2.17b$, occurring at the highest tested reduced velocity of $U^* = 12.0$ for $\epsilon = 2.5$. Furthermore, the maximum time-averaged power coefficient was observed to be 0.165 for the thinnest oblate spheroid tested, $\epsilon = 3.20$, approximately 660% higher than that observed for VIV of a sphere. This shows the relevance of geometry for FIV energy harvesting from oblate spheroids. The findings highlight the distinctive nature of FIV responses of 3D oblate spheroids compared to 2D bluff bodies such as elliptical, D-section, and square cylinders.

1. Introduction

The interaction between a structure and its surrounding fluid flow, often referred to as *fluid–structure interaction* (FSI), is of paramount significance in numerous engineering designs and applications. It is relevant to wind turbine blades, gas pipelines, and offshore structures. A salient and pervasive manifestation stemming from fluid–structure interaction is flow-induced vibration (FIV), which typically occurs when an elastic or elastically-mounted bluff body becomes stimulated into oscillatory motion due to unsteady forces imposed by the passing fluid flow. In light of potentially detrimental repercussions, FIV has been identified as a primary factor in protracted fatigue, thereby limiting the operational lifespan of a structure and, in extreme cases, precipitating catastrophic structural failure, as exemplified by the extensively documented collapse of the Tacoma Narrows Bridge in 1940. Notwithstanding

* Corresponding author.
E-mail address: adrian.corderoobando@monash.edu (A. Cordero Obando).

https://doi.org/10.1016/j.jfluidstructs.2024.104137
Received 26 October 2023; Received in revised form 15 April 2024; Accepted 14 May 2024

the potential detrimental effects of structural vibration in numerous engineering applications, it is noteworthy to underscore its dual nature, wherein it may also be a viable energy source for energy harvesting applications.

To date, numerous studies have been conducted to investigate FIV of bluff bodies possessing geometric symmetries, including circular cylinders (e.g. Brooks, 1960; Feng, 1968; Khalak and Williamson, 1996; Govardhan and Williamson, 2000; Bearman, 2011), and spheres (e.g. Jauvtis et al., 2001; Govardhan and Williamson, 2005; Sareen et al., 2018a). This work aims to gain fundamental insight into underlying FSI mechanisms that govern particular FIV responses. Notably, two prevalent body-oscillator phenomena typical of FIV are *vortex-induced vibration* (VIV) and *galloping*. Comprehensive reviews are provided in articles focused on VIV (Bearman, 1984; Sarpkaya, 2004; Williamson and Govardhan, 2004; Gabbai and Benaroya, 2005), and in books covering FIV in general (Blevins, 1990; Naudascher and Rockwell, 2005; Païdoussis et al., 2010). From a fundamental point of view, VIV is associated with the periodic shedding of vortices from both sides of an elastic or elastically mounted body. This, in turn, exerts unsteady forces on the body inducing structural vibration. If the vortex shedding frequency is close to the natural frequency of the structural system, a phenomenon known as synchronization or "lock-in" can result. In these circumstances, the frequency of vortex shedding synchronizes with (or locks onto) the frequency of body vibration, resulting in substantial body vibration due to resonance. On the other hand, galloping is often referred to as a movement-induced vibration driven by aerodynamic instability (see Naudascher and Rockwell, 2005). This instability arises from the body motion, resulting in aerodynamic forcing in the same direction as the body motion, thus supporting the oscillatory movement (see Nemes et al., 2012; Zhao et al., 2018c, 2019). Structures lacking axial symmetry (e.g., ice-coated transmission cables in winds (see den Hartog, 1932)) may be susceptible to *galloping*, either independently or in conjunction with VIV (see Bearman et al., 1987; Nemes et al., 2012; Zhao et al., 2014, 2018a; Lo et al., 2023). This susceptibility depends on structural properties (such as body geometry, mass ratio, and damping ratio), and flow conditions (such as flow-reduced velocity).

Of interest to the present study is the cross-flow FIV responses of oblate spheroids with cross-sectional aspect ratios varying between 1 and 3.20. Here, the aspect ratio is defined by $\epsilon = b/a$, where a and b are the major body diameters in the streamwise and cross-flow (transverse) directions, respectively, of an oblate spheroid placed at zero incidence angle. The recent findings of Lo et al. (2023) showed that FIV of an elliptical cylinder with an elliptical ratio of $\epsilon = 5.0$ exhibited substantial body vibration amplitudes up to $7.8b$, suggesting tremendous potential for FIV energy harvesting.

While there has been a considerable number of studies conducted on FIV of two-dimensional (2D) elliptical cylinders (e.g., Franzini et al., 2009; Navros et al., 2014; Leontini et al., 2018; Zhao et al., 2019; Lo et al., 2023), much less attention has been directed to FIV of three-dimensional (3D) oblate spheroids. Thus, a notable gap exists in the literature concerning the influence of aspect ratio on the FIV response of oblate spheroids. Furthermore, since the pioneering study on FIV energy harvesting conducted by Bernitsas et al. (2008), there has been a growing body of research aimed at exploring novel approaches for FIV-based energy harvesting devices.

Therefore, to fill this gap in the existing body of research, this study aims to provide a comprehensive understanding of how aspect ratio impacts the FIV response of oblate spheroids within the range of $1 \leqslant \epsilon \leqslant 3.20$. Additionally, we aim to evaluate the potential of spheroid FIV for energy harvesting performance.

This article describes the fluid–structure system modeling and experimental details in Section 2. The results and discussion, including FIV responses and FIV energy harvesting performance of all tested spheroids, are presented in Section 3. Finally, conclusions are drawn in Section 4.

2. Experimental methodology

2.1. Modeling of the fluid–structure system

The fluid–structure system is represented by a linear mass–spring–damper oscillator system subject to an oncoming free-stream flow. As illustrated in Fig. 1, the body oscillator is constrained to move only in the cross-flow (y) direction, and the governing equation of motion can be expressed as

$$m\ddot{y} + c\dot{y} + ky = F_y, \tag{1}$$

where m denotes the total oscillating mass, c represents the structural damping, k is spring stiffness, y is the transverse displacement and F_y represents the total transverse fluid force.

2.2. Experimental details

The present experiments were conducted in a recirculating water channel facility within the *Fluids Laboratory for Aeronautical and Industrial Research (FLAIR)* at Monash University (Australia).

Fig. 2 presents a three-view schematic of the experimental set-up, and Fig. 3 shows photographs of the corresponding three views, illustrating key components of the set-up.

This study involved five oblate spheroid models covering a range of aspect ratio, $\epsilon \in \{1.0, 1.5, 2.0,\ 2.5, 3.20\}$. These spheroid models were manufactured from Renshape 460, a medium-high density polyurethane with an identical major cross-sectional axis length of $b = 50 \pm 0.20$ mm. The different aspect ratios were achieved by modifying the streamwise diameter a, thereby varying the afterbody of the spheroids. Here, the afterbody is defined as the portion of the bluff body located downstream of flow separation points (Brooks, 1960; Bearman et al., 1987; Zhao et al., 2018a).

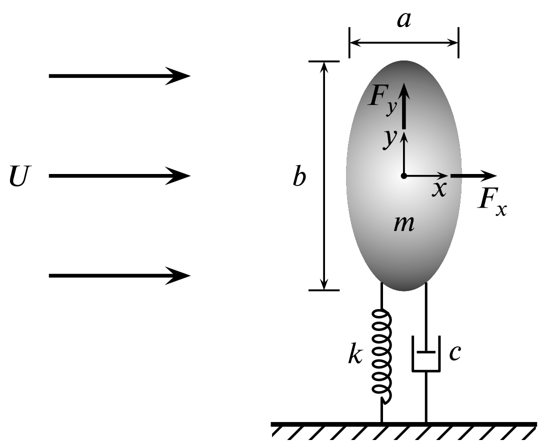

Fig. 1. Schematic of the problem studied: an oblate spheroid is elastically mounted and constrained to oscillate transversely to the oncoming freestream. Here, c is the structural damping factor; k is structural stiffness; m is the total oscillating mass; U is the free-stream velocity. The fluid forces, F_x and F_y, are the streamwise and transverse forces, respectively, acting on the body.

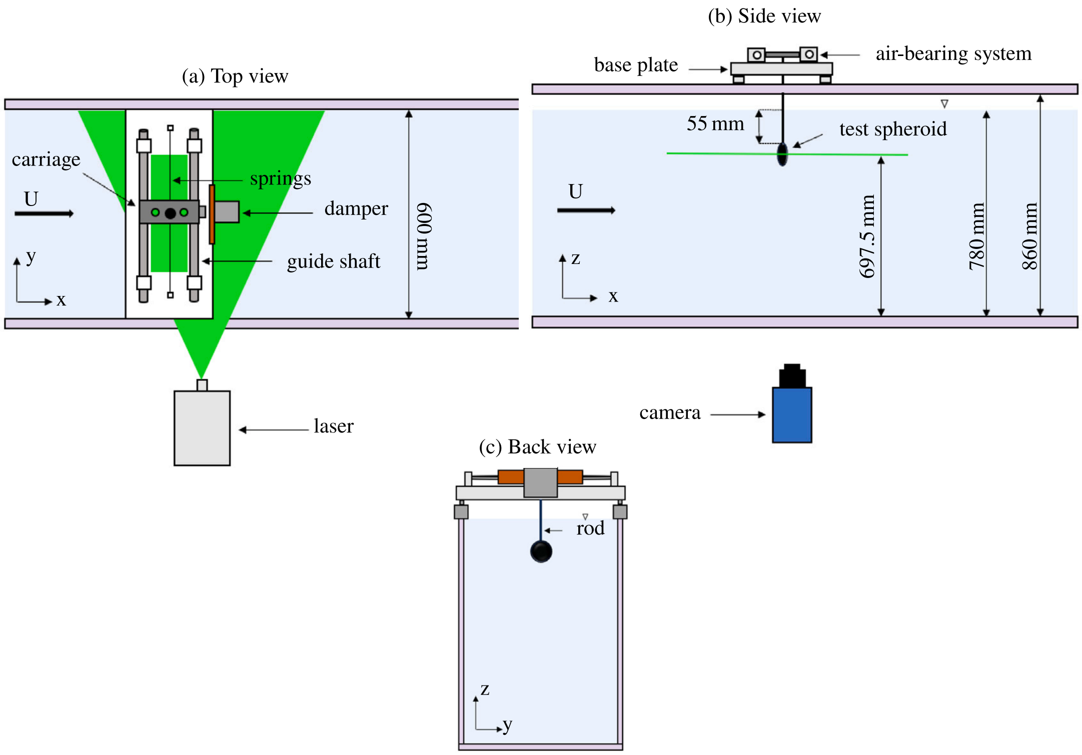

Fig. 2. A schematic showing the experimental setup in (a) top view, (b) side view, and (c) back view.

The spheroids were vertically supported by a steel rod with a diameter of 2 mm, resulting in a diameter ratio of 25 between the major diameter of the spheroid and the support rod. The distance between the upper part of the surface spheroid and the free surface was set to 55 mm, giving an immersion depth of the spheroid of $h = 1.1b$. This fully submerged configuration limits the free-surface effects, as previously demonstrated by Sareen et al. (2018b), Rajamuni et al. (2021) for the case of a sphere. The support rod was vertically integrated into a low-friction air-bearing rig (see Zhao et al., 2018a, 2019). Additionally, an eddy-current-based damper device was incorporated into the air-bearing rig to adjust the structural damping. Further details of this damper device can be found in the studies of Soti et al. (2018), Zhao et al. (2022a), Han et al. (2023a).

Table 1 presents the structural properties of the five spheroid models under investigation, encompassing aspect ratio (ϵ), geometric dimensions (a and b), total oscillating mass (m), displaced fluid mass ($m_d = 4\pi a^2 b/3$), and structural damping ratio with

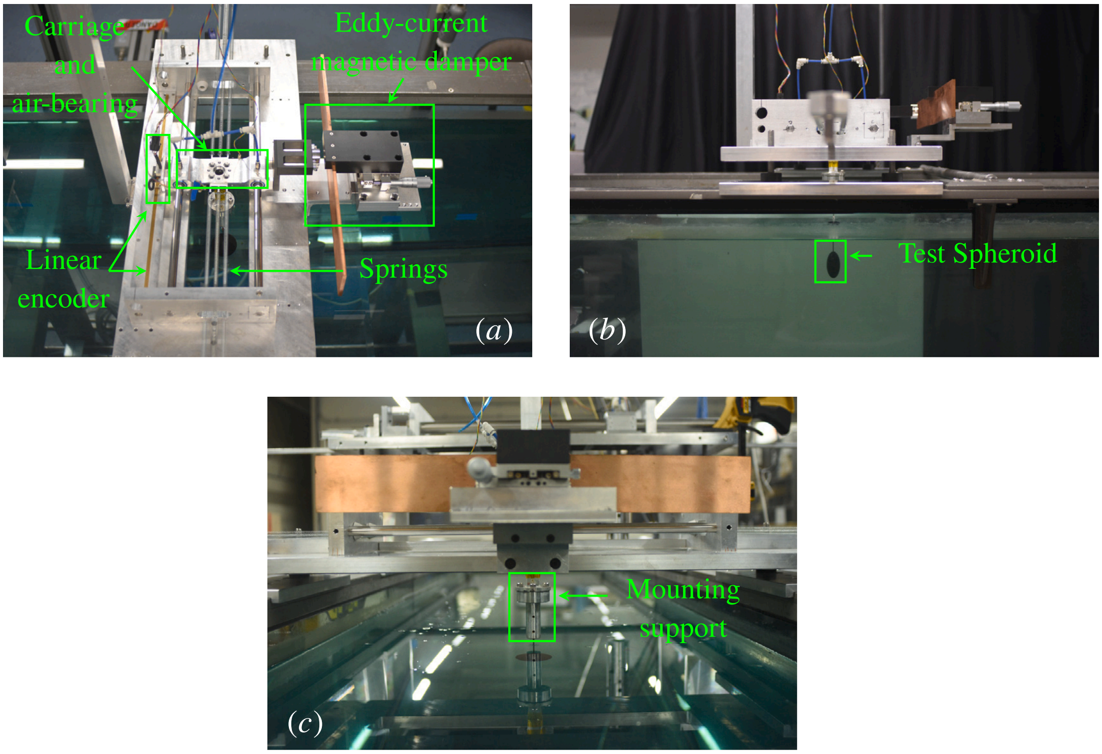

Fig. 3. Photographs showing the experimental set-up in (a) top view, (b) side view, and (c) back view.

Table 1
Structural properties for the oblate spheroids tested.

ϵ	b [mm]	a [mm]	m [g]	m_d [g]	m^*	C_A	ζ	f_{na} [Hz]	f_{nw} [Hz]
1.00	50.00	50.00	837.50	65.40	12.81	0.590	0.0195	0.685	0.669
1.53	50.00	32.50	824.30	42.50	19.40	0.482	0.0140	0.687	0.679
2.00	50.00	25.00	815.10	32.60	25.00	0.446	0.0105	0.693	0.687
2.50	50.00	20.00	809.50	26.10	31.02	0.381	0.00801	0.687	0.683
3.20	50.00	15.62	804.80	20.40	39.45	0.337	0.00545	0.706	0.703

Table 2
Values of the mass-damping parameter for all oblate spheroids tested.

ϵ	$(m^* + C_A)\zeta$
1.00	0.2613
1.53	0.2783
2.00	0.2671
2.50	0.2515
3.20	0.2725

consideration of added mass effects ($\zeta = c/(2\sqrt{k(m + m_A)})$). Additionally, it provides the natural frequencies in quiescent air (f_{na}) and water (f_{nw}). As shown in Table 2, a nearly constant mass-damping parameter, $(m^* + C_A)\zeta$ = 0.2516–0.2772, was employed to facilitate a close comparison between results across the five different aspect ratios. In this expression, the mass ratio is represented as $m^* = m/m_d$, and the added mass coefficient is defined by $C_A = m_A/m_d$, with $m_A = ((f_{na}/f_{nw})^2 - 1)m$ representing the assumed added mass in potential flow (see Lighthill, 1986; Govardhan and Williamson, 2000). The natural frequencies f_{na} and f_{nw}) were determined through free-decay tests conducted in still air and water, respectively.

2.3. Data acquisition and processing methods

The data acquisition was achieved via a computer workstation equipped with a multi-function data acquisition device (USB-6218, National Instruments, USA) and customized LabVIEW software applications. This allowed control of the water flow speeds and automation of experimental measurements.

The body displacement was measured using a linear encoder (model: RGH24; Renishaw, UK) with a resolution of 1 μm, over a linear range of ±200 mm. From the well-resolved displacement signal, the total transverse force F_y was derived based on the governing equation of motion in (1). Zhao et al. (2014, 2018b, 2022b) has validated this method for determining the transverse force.

To visualize the flow dynamics in the near wake of the immersed oblate spheroids, particle image velocimetry (PIV) measurements were conducted in the equatorial plane. Micro-hollow spheres with a diameter of 13 μm, and a specific weight of 1.1 g cm^{-3} were added into the flow to quantify the planar wake vorticity fields. A 5 W continuous laser beam (model: MLL-N-532-5 W, China) that produced a 3 mm thick laser sheet was used to illuminate particles in the horizontal plane (i.e., the x-y plane). To capture the wake structure, a high-speed camera (model: Dimax S4, PCO AG) with a resolution of 2016 × 2016 pixel^2 was used with a 52 mm Nikon lens. This gave a magnification factor of 5.42 pixels/mm. To process the photos and extract the velocity and vorticity fields, in-house software developed and validated by Fouras et al. (2008) was employed to correlate interrogation windows of size 16 × 16 pixel^2 with an overlap of 50% to obtain velocity fields. This corresponded to a velocity vector field of 125 × 125 vectors for the x-y plane.

In the present experiments, the imaging of the near wake was conducted with a sampling rate of 60 Hz for a total of 6200 image pairs in each dataset. To study the evolution of the vorticity structures in the wake, the vector fields were sorted into 48 bins based on the spheroid displacement, resulting in more than 60 image frames for each phase bin. To highlight the larger-scale structures of interest in this study, the phase-averaged vorticity fields were slightly smoothed using Gaussian smoothing to remove short-length scale structures.

The dynamic response was investigated over a range of reduced velocities, specifically within $3.0 \leqslant U^* = U/(f_{nw}b) \leqslant 12.0$, where U represents the free-stream velocity. The corresponding Reynolds number range was $4730 \leqslant Re = Ub/\nu \leqslant 20\,120$, with ν denoting the kinematic viscosity of the fluid. Furthermore, all measurements were acquired at a sampling frequency of 100 Hz, encompassing more than 60 vibration cycles.

3. Results and discussion

The main objective of this study is to investigate the effect of aspect ratio ($1.00 \leqslant \epsilon \leqslant 3.20$) on the FIV response of oblate spheroids. This section presents the vibration amplitude and frequency responses, variations of fluid force coefficients, and their relative phases with respect to the body displacement as a function of reduced flow velocity. Additionally, flow visualizations from PIV measurements of the near wake are included to help differentiate between vibration modes based on the wake structures. Furthermore, the potential implications for FIV energy harvesting performance is presented.

3.1. Vibration amplitude and frequency responses

Fig. 4 shows the normalized vibration amplitude responses ($A^*_{10} = A_{10}/b$) as a function of reduced velocity (U^*) for the five aspect ratios: $\epsilon \in [1.00, 1.53, 2.00, 2.50, 3.20]$. Here, A_{10} denotes the average of the top 10% amplitude peaks. Along with this, the corresponding logarithmic-scale power-spectral density (PSD) contours depicting the normalized body vibration frequency responses (i.e., $f^*_y = f_y/f_{nw}$) are also provided. To gain further insight into the fluid forcing frequency and FIV response regimes, Figs. 5 and 6 present corresponding PSD contours of the normalized lift frequency (i.e., $f^*_{C_y} = f_{C_y}/f_{nw}$) and the normalized vortex force frequency (i.e., $f^*_{C_v} = f_{C_v}/f_{nw}$), respectively. The PSD contour plots are constructed by applying a Fourier transform (FT) of the time series at each reduced velocity, U^*. Subsequently, the resulting spectrum is normalized by the maximum power component. An advantage of the normalization is that the dominant frequencies at any value of U^* are visible on the plot, as well as depicting changes in the frequencies as a function of U^*. This process is repeated for every U^*, and eventually, the contour plot is achieved by stacking the spectra. More details on how these PSD contour plots are computed can be found in Zhao et al. (2014).

Moreover, Fig. 7 shows the root-mean-square (rms) coefficients of the total transverse and vortex forces varying with reduced velocity, which are denoted by $C^{rms}_y = F_y/(\frac{1}{8}\rho U^2 \pi b^2)$ and $C^{rms}_v = F_v/(\frac{1}{8}\rho U^2 \pi b^2)$, respectively, for the five aspect ratios under investigation. Additionally, the relative phases of these fluid forces to body displacement are presented: the total phase (ϕ_t) signifies the phase angle between the total transverse force (F_y) and the body displacement (y), and the vortex phase (ϕ_v) represents the phase angle between the vortex force (F_v) and the body displacement (y).

The instantaneous relative phase angles between the fluid force components and the oblate spheroids displacements were calculated using the Hilbert transform (HT) (Hahn, 1996), following the same procedure outlined by Khalak and Williamson (1999), Zhao et al. (2014). Analyzing the phases to identify distinct vibration regimes has been extensively used in FIV studies of two-dimensional bluff bodies (e.g. Bishop and Hassan, 1964, Bearman and Currie, 1979, Gu et al., 1994, Govardhan and Williamson, 2000), and three-dimensional bodies (e.g. Govardhan and Williamson, 2005, Sareen et al., 2018a, McQueen et al., 2020). These studies have illustrated that either a jump or rapid change in the phases occurs when the dynamic response of the oscillating bluff body is typically associated with a change in the mode of vortex formation within the synchronization region. In particular, Govardhan and Williamson (2005) demonstrated that the transition between vibration modes (i.e., Mode I and Mode II) in the case of the elastically mounted (or tethered) sphere can be attributed to a jump in the vortex phase, ϕ_v.

In the present study, different FIV response modes are identified through an overall assessment of the vibration response, frequency response and fluid forces (specifically, the transverse lift and vortex force), coefficients of the fluid forces, and the relative phases of fluid forces to body displacement.

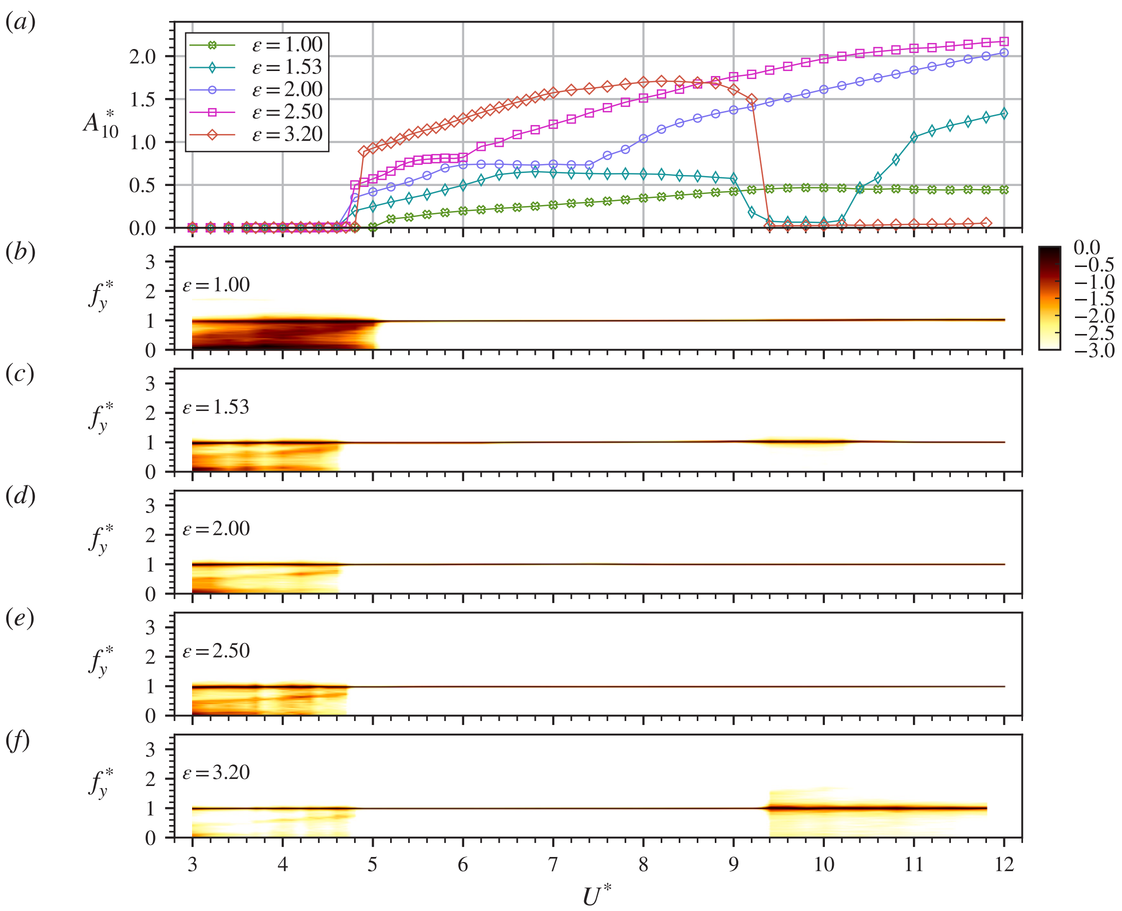

Fig. 4. Variation of the vibration amplitude response (A^*_{10}) as a function of the reduced velocity (U^*), for various aspect ratios (ϵ). Power spectrum contours of the normalized body vibration frequency (f^*_y) are shown in (b)-(f) individually for each ϵ case.

It is worth noting that the values of the mass-damping parameter, $(m^* + C_A)\zeta$, are maintained nearly constant across all ϵ cases (as indicated in Table 2) to focus on the influence of aspect ratio.

From Fig. 4(a), it is evident that the amplitude response exhibits a strong dependency on the aspect ratio. In the sphere case ($\epsilon = 1.00$), the present results for the amplitude and frequency response, in general, agree well with previous experimental studies of VIV of spheres conducted by Govardhan and Williamson (2005), Sareen et al. (2018a), despite differences in Reynolds numbers and mass ratios across these studies. In this case, the frequency response indicates the presence of a sustained lock-in region of VIV occurring at $U^* \simeq 5.0$ and persisting up to the highest examined reduced velocity $U^* = 12.0$. Within this region, the body vibration frequency is synchronized with the vortex shedding frequency, as reflected by both the frequency responses of the total transverse and vortex forces (i.e. $f^*_y = f^*_{C_y} = f^*_{C_v}$) in Figs. 5($b$) and 6($b$), respectively.

Following analyses of the total and vortex phases of Govardhan and Williamson (2005), Sareen et al. (2018a), the lock-in region is divided into distinct sub-regions: Mode I, Mode II and a transition region between these two modes. Mode I starts at the onset of the lock-in region, with the vortex phase (ϕ_v) increasing from $\sim 50°$ to $\sim 100°$ at $U^* \approx 7.6$ as it reaches the transition region (see Fig. 7(d)). As U^* is further increased in the transition region, the vortex phase sees a continuous increase to a plateau of $\sim 150°$ commencing at $U^* \approx 11$, signifying transition to Mode II.

Additionally, Fig. 7(a, b) show the variations of C_y^{rms} and C_v^{rms} as a function of U^*. It can be seen that C_y^{rms} exhibits an abrupt jump up at the beginning (the onset of lock-in) of Mode I and subsequently decreases steadily as the response transitions to Mode II. Furthermore, a global maximum for C_v^{rms} is observed at $U^* = 10$, corresponding to the largest vibration in Mode II. These results are consistent with previous experiments on VIV of an elastically mounted sphere (e.g., Govardhan and Williamson, 2005; Sareen et al., 2018a).

Remarkably, with the deformation of the sphere into an oblate spheroid with $\epsilon = 1.53$, while observing both Mode I and Mode II as for the sphere case, a distinct galloping-dominated response regime, denoted by G-I, emerges at high reduced velocities beyond 10.2, followed by a desynchronization region.

For this ϵ, as illustrated in Figs. 5(c) and 6(c), Mode I occurs over the reduced velocity range of $4.7 \leqslant U^* \leqslant 6.5$, where the dominant frequencies of the fluid forces, $f^*_{C_y}$ and $f^*_{C_v}$, are synchronized with the body displacement frequency, namely $f^*_{C_y} \cong f^*_{C_v} \cong f^*_y$.

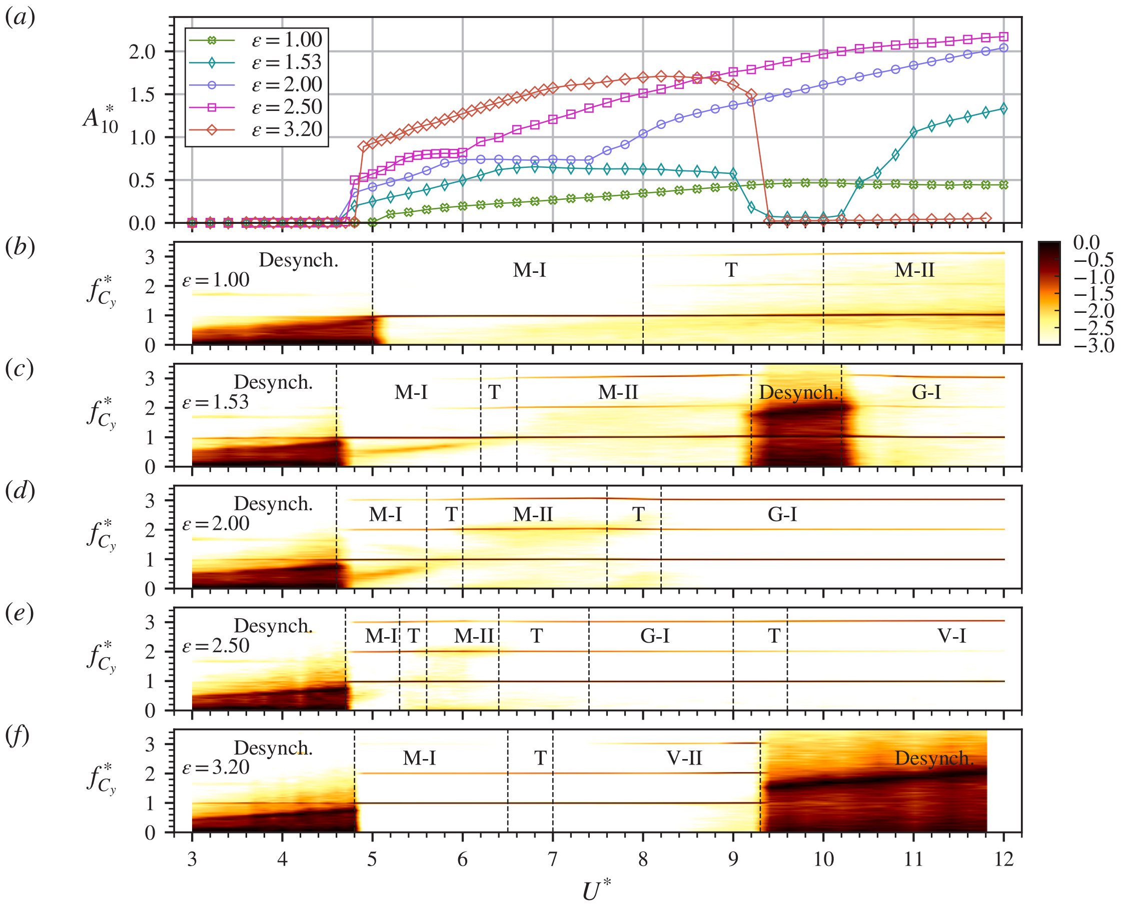

Fig. 5. Variation of the vibration amplitude response (A^*_{10}) as a function of the reduced velocity (U^*), for various aspect ratios (ϵ). Power spectrum contours of the normalized transverse lift frequency ($f^*_{C_y}$) are shown in (*b*)-(*f*) individually for each ϵ case. M-I: pure VIV Mode-I; M-II: pure VIV Mode-II; V-I : VIV-dominated V-I mode; V-II : VIV-dominated V-II mode; G-I: Galloping-dominated-I; T: Transition.

Additionally, as displayed in Fig. 7, the onset of Mode I is associated with a sharp jump in the r.m.s. values of the fluid force coefficients (C_y^{rms} from 0.05 to 0.22, and C_v^{rms} from 0.05 to 0.18). It can be observed that the values of the fluid force phases remain almost constant over this U^* range, $\phi_t \approx 30°$ and $\phi_v \approx 50°$. The value of C_y^{rms} reaches a peak value of 0.37 at $U^* = 6.2$ before progressively reducing as the vibration mode transitions towards Mode II. In addition, there is a noticeable sharp jump in the total phase from $\phi_t \approx 30°$ at $U^* = 6.2$ to approximately 55° at $U^* = 6.6$, while the vortex phase increases from $\phi_v \approx 50°$ at $U^* = 6.2$ to approximately 75° at $U^* = 6.6$. This indicates a rapid transition between the two VIV modes, Mode I and Mode II.

Mode II covers the range of reduced velocity $6.6 \leqslant U^* \leqslant 9.2$, where C_v^{rms} remains almost constant at 0.2. In addition, it can be seen that the phases increase progressively at the start of Mode II towards their highest values: $\phi_t \approx 145°$ and $\phi_v \approx 150°$. It can also be seen in the frequency contour plots (Figs. 5–6) that in the Mode II regime, there is a change in the frequency response, with the appearance of a second-harmonic ($f^*_{C_v} = f^*_{C_y} \simeq 2$) and third-harmonic ($f^*_{C_v} = f^*_{C_y} \simeq 3$) components.

Notably, the vibration amplitudes in these two modes are significantly larger than the sphere counterparts — the local peak amplitude is observed to be $A^*_{10} = 0.7$, a 75% increase over that ($A^*_{10} \simeq 0.4$) of the sphere case. As U^* is further increased to the desynchronization region (spanning $9.2 \leqslant U^* \leqslant 10.2$), the body vibration is almost suppressed ($A^*_{10} \leqslant 0.05$), and the frequency responses of both body vibration and fluid forcing (i.e., $f^*_{C_y}$ and $f^*_{C_v}$) exhibit prevalent broadband noise following the Strouhal frequency trend for a fixed body. It is noteworthy that at the onset of the second synchronization region, there is a sudden decrease in the magnitudes of the fluid force coefficients, with C_y^{rms} dropping from 0.15 to 0.05 and C_y^{rms} from 0.22 to 0.05. Additionally, there is also a sharp jump in the phases, as shown in Fig. 7, indicating another transition in vibration modes. Upon further increase in U^*, the body vibration reemerges, marked by another jump in the magnitudes of the fluid force coefficients, along with a sharp jump in the phases, displaying a monotonically increasing amplitude trend with U^* that follows a linear growth beyond $U^* = 11$. The maximum vibration amplitude observed is $A^*_{10} = 1.33$ at the highest tested reduced velocity $U^* = 12.0$. This linear growth of A^*_{10} is associated with $\phi_t \approx 75°$ (Fig. 7(*c*)), indicating that the total transverse force leads the body velocity ($\dot{y}$) by approximately 15°, thereby favoring the enhancement of body vibration.

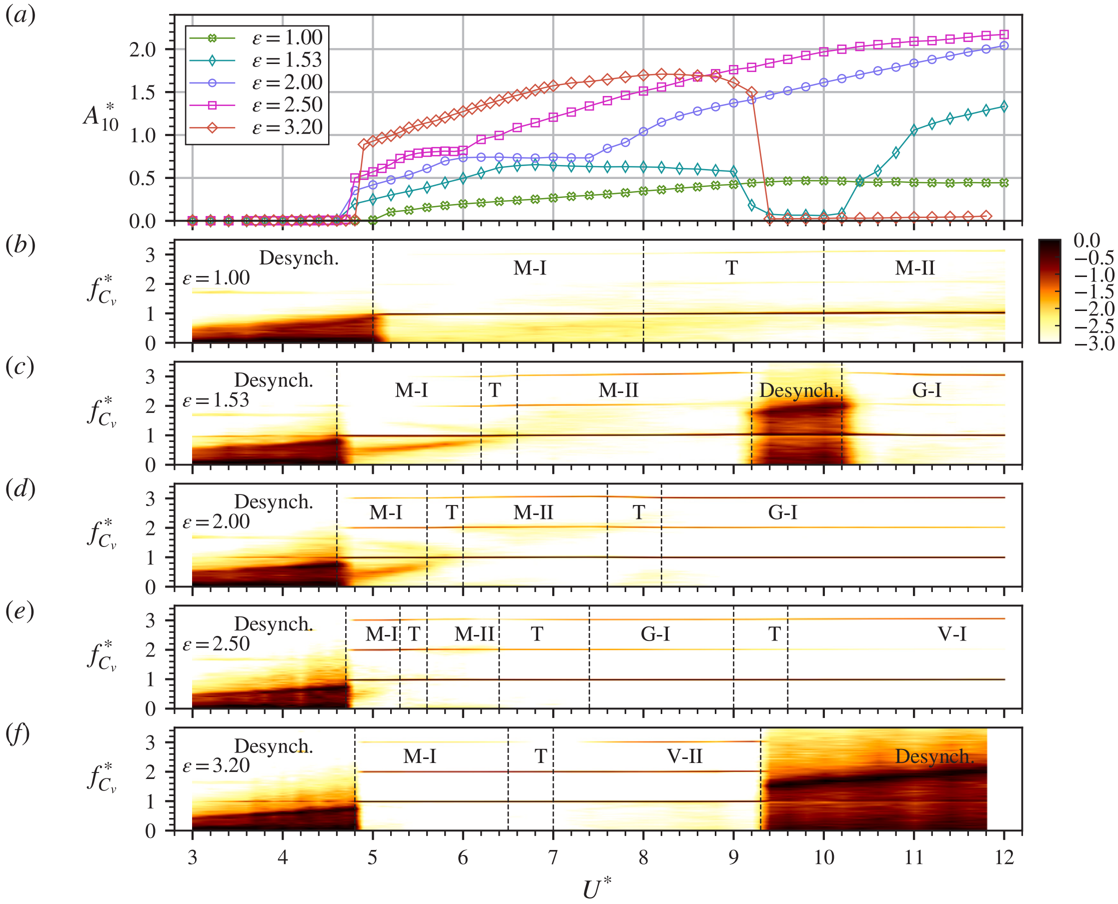

Fig. 6. Variation of the vibration amplitude response (A^*_{10}) as a function of the reduced velocity (U^*), for various aspect ratios (ϵ). Power spectrum contours of the normalized vortex force frequency ($f^*_{C_v}$) are shown in (b)-(f) individually for each ϵ case.

It is pertinent to note that galloping is categorized as a type of movement-induced excitation (MIE) (see Naudascher and Rockwell, 2005). This vibration mechanism is characterized typically by a linear increase of the vibration amplitude with increasing reduced velocity and with the dominant frequency of body vibration significantly lower than that of vortex shedding. Galloping can occur for short bluff bodies (i.e., those with a sufficiently small length-to-height ratio) placed in a cross-flow direction and possessing only one degree of freedom (1-DOF), either transverse or torsional.

Consequently, the G-I regime for $\epsilon = 1.53$ is classified as a galloping-dominated response mode. On the other hand, both frequency responses of $f^*_{C_y}$ and $f^*_{C_v}$ in Figs. 5(c) and 6(c), respectively, show a strong third harmonic component in the G-I mode, similar to the galloping response of a D-section cylinder as observed in the study of Zhao et al. (2018a). This indicates that multiple vortices are shed per body vibration cycle, suggesting that a 3D oblate spheroid may be susceptible to movement-induced vibration akin to 2D bluff bodies with axial asymmetries, such as D-sections and square cylinders. Flow visualizations are provided in Section 3.2–3.3 to show that high-order harmonic frequency components of the fluid forces are linked to a greater number of vortices shed per oscillation cycle.

It is interesting to note that in galloping response of 2D bluff bodies like D-section and square cylinders with low mass ratios (e.g., Zhao et al., 2018a; Nemes et al., 2012; Zhao et al., 2014), the dominant component of $f^*_{C_y}$ or $f^*_{C_v}$ could be its third harmonic or other higher-order harmonics. However, in the present 3D spheroid case, the dominant frequency of $f^*_{C_y}$ remains consistent with that of the body vibration f^*_y. Further investigation is required to ascertain whether the present G-I mode is driven by the same mechanism as the conventional pure galloping mode. This necessitates further work involving careful, precise force measurements on a stationary body for quasi-steady analysis (see Zhao et al., 2018a), along with a detailed examination of the 3D wake structure of the G-I response mode. Nevertheless, the G-I regime exhibits features similar to those in two-dimensional square or D-section cylinders under galloping oscillations. Here, the amplitude response displays a monotonic increase with reduced velocity beyond a certain threshold, unlike VIV, where the vibration is self-limiting (see Nemes et al., 2012; Zhao et al., 2014). The emergence of desynchronization followed by the galloping-dominated G-I regime was unforeseen, especially considering that in the sphere case, the body vibration exhibited robustness with significant amplitudes persisting up to high reduced velocities.

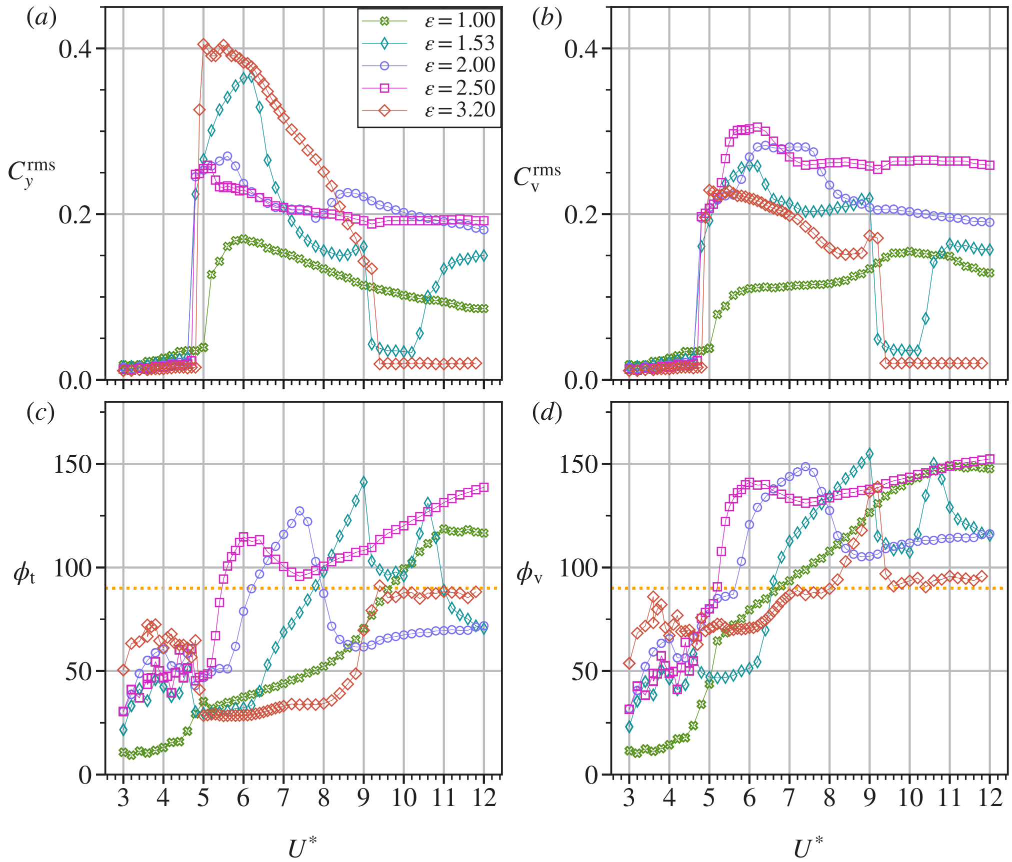

Fig. 7. Variation of the transverse lift force coefficient (C_y^{rms}) in (a), the vortex force coefficient (C_v^{rms}) in (b), the total phase (ϕ_t) in (c), and vortex phase (ϕ_v) in (d), all as functions of the reduced velocity U^*.

As the spheroid body was further deformed to $\epsilon = 2.00$ and 2.50, the amplitude and frequency responses exhibit notable differences from those observed for $\epsilon = 1.53$. As can be seen from Figs. 4–6, synchronization of the dominant frequency of the body vibration (f_y^*) and fluid forcing ($f_{C_y}^*$ and $f_{C_v}^*$) is evident for both $\epsilon = 2.00$ and 2.50, commencing with the onset of Mode I and persisting up to the highest tested reduced velocity of $U^* = 12.0$. This is distinctly different from the $\epsilon = 1.53$ case, which sees a desynchronization region occurring over $9.2 \leqslant U^* \leqslant 10.2$. Here, the (intermediate) desynchronization region exhibited by $\epsilon = 1.53$ might be caused by structural damping. Perhaps a decrease in the damping ratio could potentially eliminate the desynchronization region, resulting in a continuous transition between the VIV and the galloping-dominated regimes.

A closer examination of the $f_{C_y}^*$ and $f_{C_v}^*$ responses, as shown respectively in Figs. 5 and 6, reveals that in the case of $\epsilon = 2.00$, the synchronization region can be divided into three sub-regions associated with Mode I ($4.6 \leqslant U^* < 5.6$), Mode II ($6 < U^* < 7.4$), and G-I mode ($U^* > 7.4$). The onset of Mode I is notably characterized by a sudden jump in both C_y^{rms} and C_v^{rms} at $U^* = 4.7$ (Fig. 7). Subsequently, within the Mode I regime, C_y^{rms} reaches a global maximum value of 0.27 at $U^* = 5.6$, coinciding with the largest vibration in this regime. On the other hand, ϕ_t remains almost constant at approximately 50° throughout the entire Mode I regime. Additionally, as illustrated in Fig. 5(d) and Fig. 6(d), both $f_{C_y}^*$ and $f_{C_v}^*$ display second- and third-harmonic components, which are considerably weaker in power compared to the dominant component at the body vibration frequency.

With a further increase in the reduced velocity beyond 6, C_y^{rms} decreases progressively, indicating the transition towards Mode II. This transition region, denoted by T, can be identified by the rapid jump in the total and vortex phases over the range of $5.6 < U^* < 6.0$, where ϕ_t sharply increases from 60° to 80° and ϕ_v from 90° to 125°. Mode II regime covers the reduced velocity range of $6.00 \leqslant U^* \leqslant 7.6$, where ϕ_t continuously increases from 80° to 125° and ϕ_v from 125° to 150°. One interesting feature of Mode II is that C_v^{rms} remains almost constant at 0.20 over the entire regime.

With a further increase in U^* beyond 7.4, the FIV response f $\epsilon = 2.00$ undergoes a second transition to a galloping-dominated mode, as denoted by G-I. As can be seen in Fig. 7, this transition regime is associated with a sharp change in both the total and vortex phases over the reduced velocity range of $7.6 \leqslant U^* \leqslant 8.2$: ϕ_t drops sharply from 125° to 60° and ϕ_t from 150° to 110°. Interestingly, this transition sees the appearance of a relatively strong third harmonic and a weak second harmonic in both $f_{C_y}^*$ and $f_{C_v}^*$.

Eventually, the galloping-dominated mode (G-I) takes place for $U^* > 8.2$ in the present experiments. In this regime, the vibration amplitude increases rapidly, following a nearly linear trend with U^*. The maximum A^*_{10} value in the G-I regime is observed to be 2.04 at $U^* = 12.0$ (the highest value tested), seeing a 53% increase over $\epsilon = 1.53$. On the other hand, as shown in Fig. 5(d) and Fig. 6(d), the frequency responses of the fluid forces exhibit a weak second-harmonic component and a relatively strong third-harmonic component, while their dominant components coincide with that of the body vibration frequency.

For $\epsilon = 2.50$, the synchronization region can also be divided into various sub-regions: Mode I ($4.8 \leqslant U^* < 5.3$), Mode II ($5.6 \leqslant U^* < 6.4$), G-I mode ($7.4 \leqslant U^* < 9.0$), and V-I ($U^* > 9.6$) mode (a VIV-dominated response).

While the identifications of the Mode I, Mode-II, and G-I regimes are similar to the previous case of $\epsilon = 2.00$, the present $\epsilon = 2.50$ case sees an additional V-I mode following the G-I regime. Unlike the G-I mode, the V-I mode is characterized by the appearance of a relatively strong third harmonic ($f^* \simeq 3$) in both $f^*_{C_y}$ and $f^*_{C_v}$, but with a much weaker second harmonic ($f^* \simeq 2$) compared to the G-I mode, as shown in Figs. 5 and 6. Consequently, as depicted in Fig. 5(a), the A^*_{10} response in V-I mode displays a lower rate of increase with U^* compared to that of G-I mode, implying that the second harmonic of the fluid forcing frequency can have a favorable effect on the body vibration. This lower rate of increase is associated with a gradual increase in ϕ_t from approximately 108° at $U^* = 9$ to approximately 139° at $U^* = 12.0$, which implies that the FIV mechanism responsible for the structure vibration can be linked to a VIV-dominated response rather than a galloping-dominated response. The maximum A^*_{10} value observed in V-I mode is 2.17. Additionally, as ϵ is increased from 1.53 to 2.50, it is evident that both Mode I and Mode II regions shrink but with noticeable increases in local peak A^*_{10} values. The above results highlight that the body aspect ratio affects the FIV response in the galloping-dominated regions and in the VIV-dominated modes.

As the body aspect ratio is further increased to $\epsilon = 3.20$, representing the largest deformation from the sphere and with the smallest afterbody among all tested cases, the FIV response exhibits two synchronization regimes: Mode-I (over $4.8 \lesssim U^* \lesssim 6.5$) and V-II (over $7 \lesssim U^* \lesssim 9.3$), as illustrated in Fig. 5(f) and Fig. 6(f). The characteristics of Mode-I in this ϵ case resemble those observed for $\epsilon = 1.53$, in terms of the curve shape of the amplitude response, harmonic components in both $f^*_{C_y}$ and $f^*_{C_v}$. The vibration mode V-II displays variations of ϕ_t and ϕ_v different from the one presented by Mode II, and from their frequency responses, mode V-II is characterized because of a strong contribution of the second harmonic, which is weak for Mode II for $\epsilon = 1.53$. Additionally, as discussed in sections 3.2–3.3, the wake structure in mode V-II differs from the one displayed by mode II. However, of interest, the vibration amplitudes are substantially larger than those of $\epsilon = 1.53$. For instance, the peak amplitude is observed to be $A^*_{10} \simeq 1.70$ at $U^* = 8.0$ in V-II, representing an increase of 143% compared to the peak A^*_{10} in Mode-II for $\epsilon = 1.53$.

Furthermore, it is noteworthy that in the very recent experimental study on FIV of an elliptical cylinder with $\epsilon = 5.0$ conducted by Lo et al. (2023), a 2D elliptical cylinder with an even smaller afterbody exhibits profound combined VIV and galloping effects with substantially large amplitudes ($A^*_{10} \approx 8$) occurring at similar U^* values. This suggests that for the case of bluff bodies with a considerably reduced afterbody, the mechanisms governing the FIV of 3D thin oblate spheroids show some similarities to those of FIV of 2D thin elliptical cylinders.

In summary, the results above demonstrate a significant influence of aspect ratio on the FIV response of spheroids as a function of reduced velocity. Across all ϵ, Mode I with a pure VIV response is observed. Moreover, for the cases of $\epsilon \in [1.53, 2.00, 2.50]$, the oblate spheroids experience galloping-dominated responses above certain reduced velocities. Furthermore, the cases $\epsilon = [2.00, 3.20]$ exhibit new VIV-dominated regimes, characterized by the amplitude of vibration being higher than conventional VIV for the sphere case. The results also suggest that the mechanisms governing FIV of 3D oblate spheroids are similar from those in FIV of 2D elliptical cylinders, even though there is a significant difference between the three-dimensional flow structures of 3D spheroids and those of 2D elliptical cylinders.

3.2. VIV-dominated vortex formation modes

To gain a better understanding of the fluid–structure interaction, this subsection presents PIV measurements conducted at selected reduced velocities, as indicated in Fig. 8, serving as representative examples for the different FIV response regimes.

3.2.1. Mode-I

Fig. 9 shows phase-averaged PIV snapshots for Mode I at various reduced velocities for $\epsilon = 1.00, 1.53, 2.00, 2.50$ and 3.20. For each ϵ, as illustrated by the red points on the sine waves showing the position in the cycle, four phase-averaged PIV snapshots (selected from 48 phases) are presented in columns. The horizontal dashed lines denote the centerline of the zero flow condition, while the vertical bars denote the vibration ranges.

As illustrated in Fig. 9, all oblate spheroid cases (except for the sphere $\epsilon = 1.00$) in the Mode-I regime exhibit a 2(P+S) wake pattern, characterized by a pair (P) of opposite-sign vortices along with one single (S) vortex shed per half body vibration cycle. Note the nomenclature for the wake patterns in this study aligns with the terminology introduced by Williamson and Roshko (1988). The sphere case exhibits a 2P mode, consisting of a counter-rotating vortex pair shed during each half-body vibration cycle. This observation aligns with the previous findings on VIV of spheres as reported by Govardhan and Williamson (2005), Sareen et al. (2018a). For the oblate spheroids, for example, when $\epsilon = 1.53$, a pair (P_1) of opposite-sign vortices (depicted as anti-clockwise in red for positive and clockwise in blue for negative) along with a single (S_1) negative vortex are being shed at the body's highest vibration position; conversely, at the body's lowest vibration position in the second half vibration cycle, another pair (P_2) of opposite-sign vortices along with a single (S_2) positive vortex are shed. Despite the increase in vibration amplitude with ϵ in this response regime, the 2(P+S) wake mode remains consistently observed.

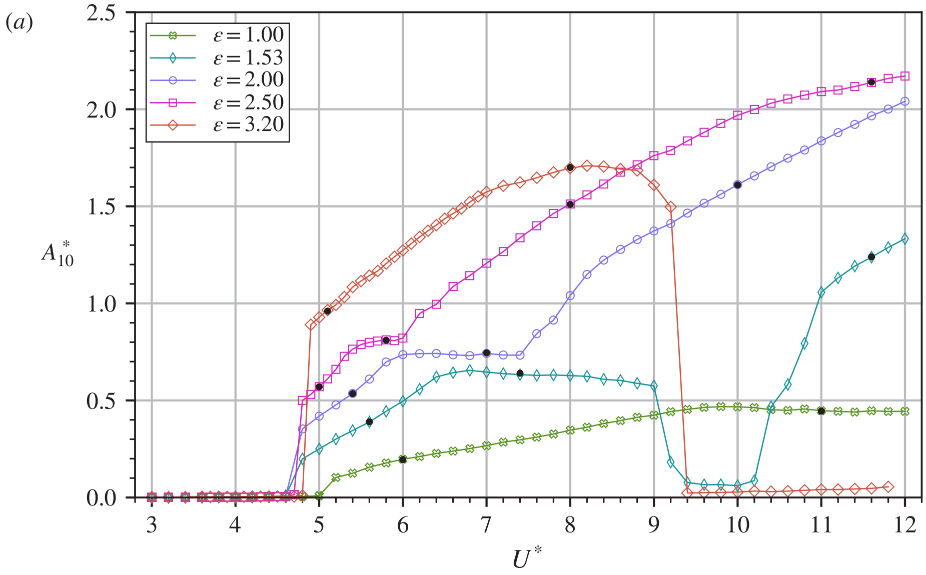

Fig. 8. Revisit of the amplitude responses as a function of reduced velocity for all the aspect ratios tested, with black dots indicating the reduced velocity values where PIV measurements were conducted for various FIV response regimes.

Fig. 10 presents sample time traces of the body displacement and the coefficients of lift and vortex forces, together with their power spectral density, for the corresponding ϵ cases in Fig. 9. As shown in the left column of Fig. 10, the time traces indicate that both C_y and C_v are generally in phase with the body displacement (y^*) for all ϵ cases. This aligns with the results in Fig. 7, where both ϕ_t and ϕ_v are less than 90° for Mode I in all ϵ cases. Interestingly, on the other hand, the PSD plots for the spheroids reveal significant second and third harmonics in both the lift and vortex forces, in contrast to the sphere case. This aligns with a change in wake mode when the sphere is deformed into the oblate spheroids.

3.2.2. Mode-II

As illustrated in Fig. 11, all oblate spheroid cases in the Mode-II regime exhibit a 2(P+S) wake pattern, which is similar to Mode I, while the sphere case displays a 2P pattern in agreement with the previous findings of Govardhan and Williamson (2005), Sareen et al. (2018a). For example, ϵ = 1.53 in Fig. 11(b) displays the wake structure at U^* = 7.40. It can be observed that the wake deflection angle increases and the shear layers become more elongated than in the Mode I case (Fig. 9(b)). As the oblate spheroid ascends, a clockwise vortex (S_1) forms from the upper shear layer, followed by counter-rotating vortices (P_1). Similarly, during the downward motion, an anti-clockwise vortex (S_2) forms from the lower shear layer, followed by another pair (P_2). This mode exhibits a 2(P+S) wake pattern per oscillation cycle, differing from Mode I primarily in the timing of the vortical structure formation.

Additionally, Fig. 12 demonstrates that all non-unity ϵ cases share common features in the time traces of the fluid forces. As it can be seen, both the lift and vortex forces are notably out of phase with the body displacement, differing from the Mode-I cases in Fig. 10. On the other hand, the PSD plots shows the presence of multiple peaks related to the harmonic components of $f^* \simeq 2$ and 3. Interestingly, the second and third harmonic contributions are equally powerful in this vibration regime. Despite the increase in vibration amplitude with ϵ in this response regime, the 2(P+S) wake mode remains consistently observed for oblate sphere wakes.

3.2.3. Mode V-I

Figs. 13 shows a 6P pattern observed in PIV sample measurements for ϵ = 2.50 at U^* = 11.60 within the V-I regime. Unlike Modes I and II, this VIV-dominated regime displays a distinctly different wake mode characterized by three pairs (P) of counter-rotating vortices shed per half oscillation cycle, termed the 6P mode. Particularly noteworthy are significant changes in the power spectra of C_y and C_v, as shown in Fig. 14, where their third harmonics appear to be much stronger than their second harmonics, which is distinct from Modes I and II. On the other hand, the periodic time traces of C_y and C_v indicate an out-of-phase relationship (≈ 140° in Fig. 7) with the body displacement, implying that this 6P wake mode is associated with a VIV response, rather than a galloping response.

3.2.4. Mode V-II

Figs. 15 shows the sample PIV measurements for ϵ = 2.50 at U^* = 11.60 within the V-II regime. As illustrated, this wake mode displays a 2(2P+S) pattern, consisting of two pairs (P) of counter-rotating vortices and one single vortex (S) shed per half oscillation cycle. In addition, from Fig. 16, both the lift and vortex forces exhibit harmonic components at $f^* \approx 2$ and 3, with their second harmonic being the second strongest frequency component. On the other hand, the profile of the lift (C_y) is nearly in-phase

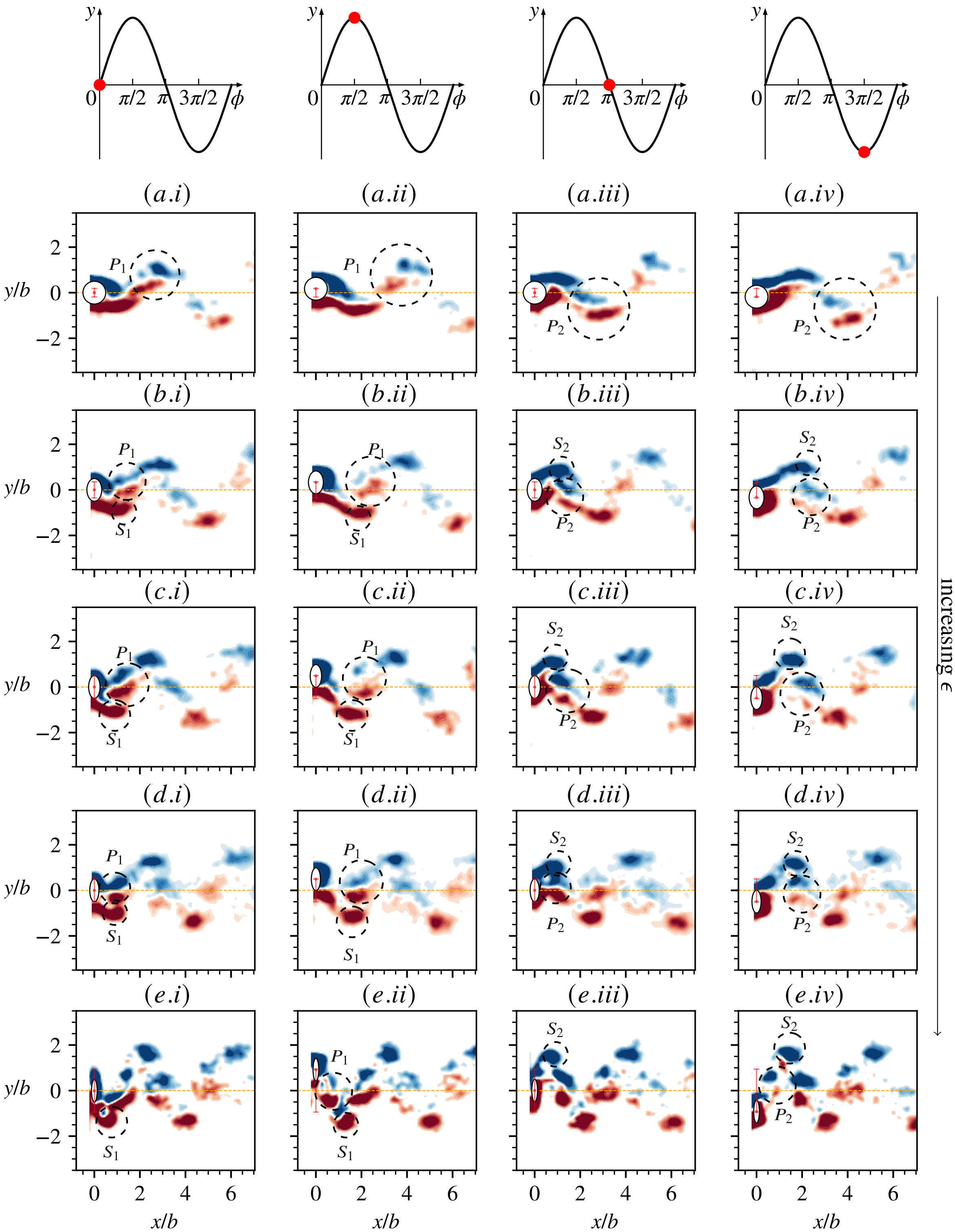

Fig. 9. Wake patterns visualized from PIV spot measurements in the Mode-I regime for all ϵ cases: (a) $\epsilon = 1.00$, $U^* = 6.00$, (b) $\epsilon = 1.53$, $U^* = 5.60$, (c) $\epsilon = 2.00$, $U^* = 5.40$, (d) $\epsilon = 2.50$, $U^* = 5.00$, and (e) $\epsilon = 3.20$, $U^* = 5.10$. The normalized vorticity range is $\omega^* = \omega D/U \in [-3, 3]$, with ω being the vorticity.

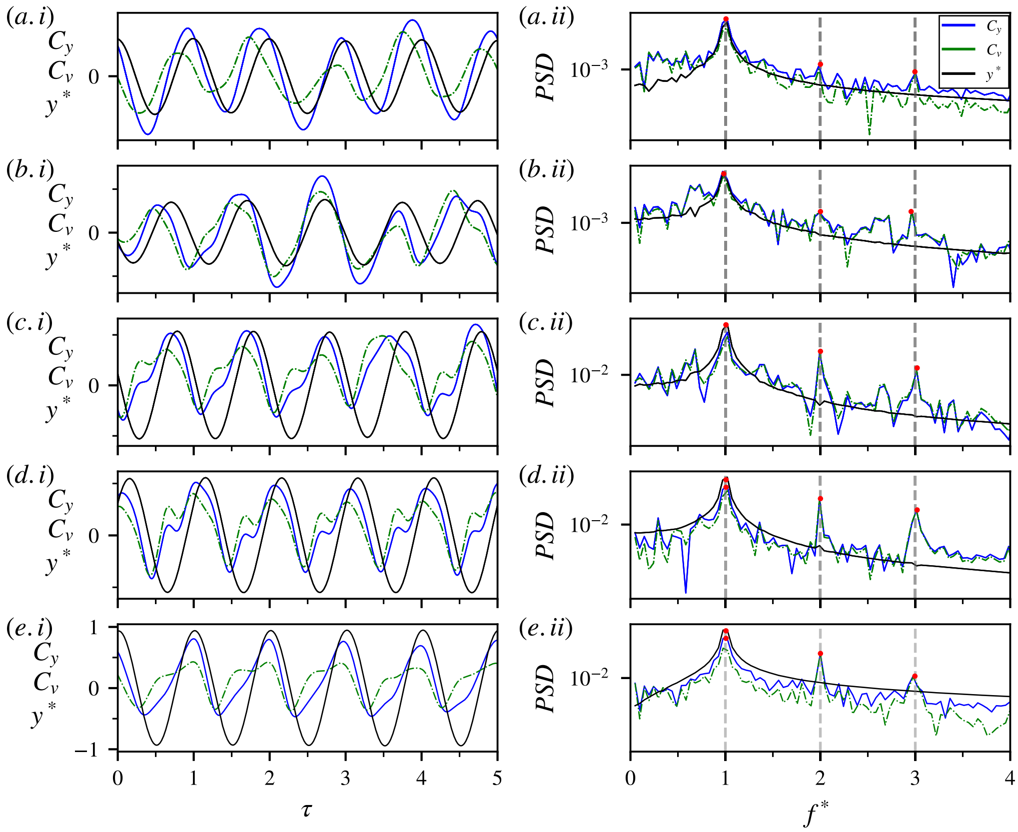

Fig. 10. Sample time traces of the body displacement (y^*), and the coefficients of the total transverse force (C_y) and the vortex force (C_v) within the Mode-I regime, along with the corresponding PSD plots for (*a*) $\epsilon = 1.00$ at $U^* = 6.00$, (*b*) $\epsilon = 1.53$ at $U^* = 5.60$, (*c*) $\epsilon = 2.00$ at $U^* = 5.40$, (*d*) $\epsilon = 2.50$ at $U^* = 5.00$, and (*e*) $\epsilon = 3.20$ at $U^* = 5.10$. Note that the time traces are plotted as a function of the dimensionless time $\tau = tf_{nw}$ and the power spectrum as a function of f^*. The red dots in the power spectrum indicate multiple harmonic contributions. (For interpretation of the references to color in this figure legend, the reader is referred to the web version of this article.)

with the body vibration ($\phi_t \approx 40°$), while the vortex force is considerably out-of-phase with the body vibration ($\phi_v \approx 90°$). These characteristics are distinct from those observed in the V-I mode for $\epsilon = 2.50$. Nevertheless, due to the lift force being predominantly in phase with the body displacement, this wake mode is considered a VIV-dominated mode.

In summary, the PIV measurements together with frequency analysis reveal changes in the wake mode in different FIV response regimes for the spheroids. It has been demonstrated that all the elliptical ratios tested ($1.00 \leqslant \epsilon \leqslant 3.20$) display a pure VIV mode - Mode I. Furthermore, the second VIV mode, Mode II, was observed to occur for the cases of $1.00 \leqslant \epsilon \leqslant 2.50$. Interestingly, two additional VIV-dominated modes were observed to occur: a V-I mode for $\epsilon = 2.50$ and a V-II mode for $\epsilon = 3.20$. The V-I mode manifests as a 6P pattern, associated with the dominant frequency at $f^* \simeq 1$ and second strongest component at $f^* \simeq 3$ in both $f^*_{C_y}$ and $f^*_{C_v}$. Conversely, the V-II mode displays a 2(2P+S) pattern, with the second harmonic ($f^* \simeq 2$) being the second strongest component in both $f^*_{C_y}$ and $f^*_{C_v}$.

3.3. Galloping-dominated vortex formation mode: Mode G-I

Fig. 17 presents sample PIV vorticity fields for representative cases within the galloping-dominated G-I regime for $\epsilon = 1.53$ at $U^* = 11.60$, $\epsilon = 2.00$ at $U^* = 10.00$, and $\epsilon = 2.50$ at $U^* = 8.00$. All cases here are observed to exhibit a 2(2P+S) wake pattern, characterized by two pairs (P) of opposite-sign vortices and a single vortex shed per half-body vibration cycle. Compared to the previous VIV-dominated modes, a notable increase in the elongation of shear layers coupled with large body vibrations is observed. It can be observed that there is a strong interaction between elongated and opposite sign shear layers, resulting in a high number of vortical structures shed per oscillation cycle.

Fig. 18 shows sample time traces of the structural and fluid dynamics corresponding to the above PIV cases. In all cases, both C_y and C_v display their dominant frequency matching the body vibration frequency at $f^* \simeq 1$, along with a significant third harmonic component at $f^* \simeq 3$. This frequency response is similar to the case of the V-I regime for $\epsilon = 2.50$ at $U^* = 11.60$ (Fig. 14). Despite the similarity in the 2(2P+S) pattern observed in V-II and G-I modes, the total phase ϕ_t is found to be approximately 100°, suggesting

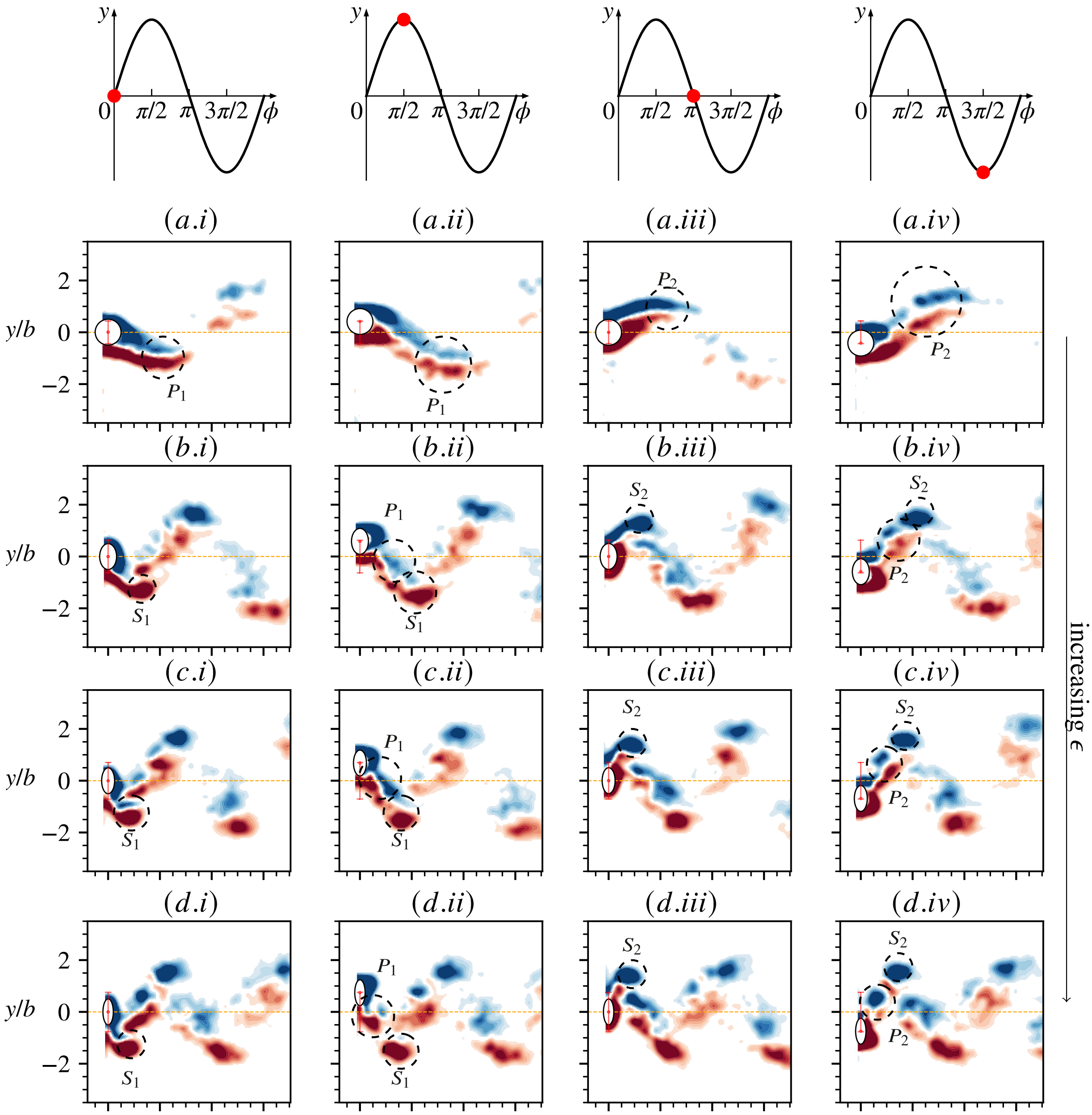

Fig. 11. Wake patterns visualized from PIV spot measurements in the Mode-II regime for all ϵ cases: (*a*) $\epsilon = 1.00$, $U^* = 11.00$, (*b*) $\epsilon = 1.53$, $U^* = 7.40$, (*c*) $\epsilon = 2.00$, $U^* = 7.00$, and (*d*) $\epsilon = 2.50$, $U^* = 5.80$. The normalized vorticity range is $\omega^* = \omega D/U \in [-3, 3]$. A 2(P+S) pattern is observed in PIV spot measurements in the Mode-II regime for all oblate spheroid cases in (*b*)–(*d*).

that the transverse lift is nearly in phase with the body movement velocity, favoring body vibration and leading to a galloping response.

3.4. Potential implications for FIV energy harvesting performance

This subsection evaluates the potential FIV energy harvesting performance for the spheroids tested. In practice, power extraction from cross-flow FIV involves using a power generator that functions as a damper. The instantaneous power output of the energy harvester based on cross-flow FIV is given by $P = \mathbf{F}_y \cdot \dot{\mathbf{y}}$, and the dimensionless power output coefficient for an oblate spheroid can be defined by

$$C_P = P\Big/\left(\frac{1}{2}\rho U^{*3}\pi(b^2/4)\right). \tag{2}$$

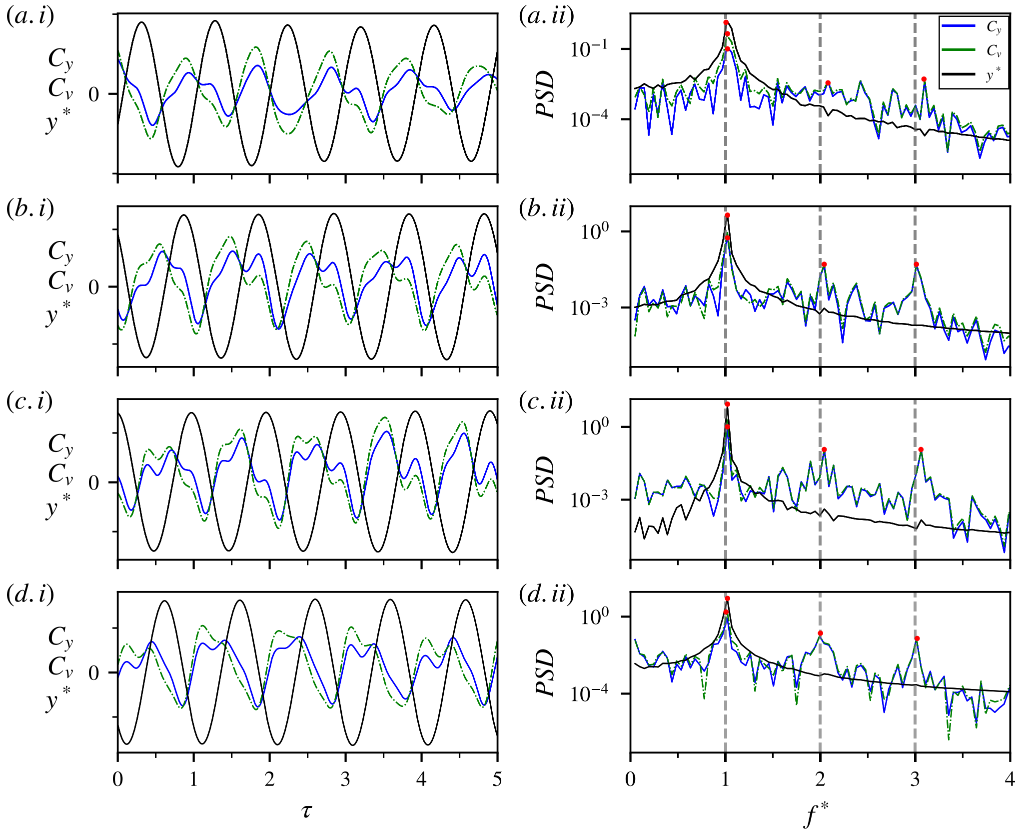

Fig. 12. Sample time traces of the body displacement (y^*), and the coefficients of the total transverse force (C_y) and the vortex force (C_v) within the Mode-II regime, along with the corresponding PSD plots for (a) $\epsilon = 1.00$ at $U^* = 11.00$, (b) $\epsilon = 1.53$ at $U^* = 7.40$, (c) $\epsilon = 2.00$ at $U^* = 7.00$, and (d) $\epsilon = 2.50$ at $U^* = 5.80$.

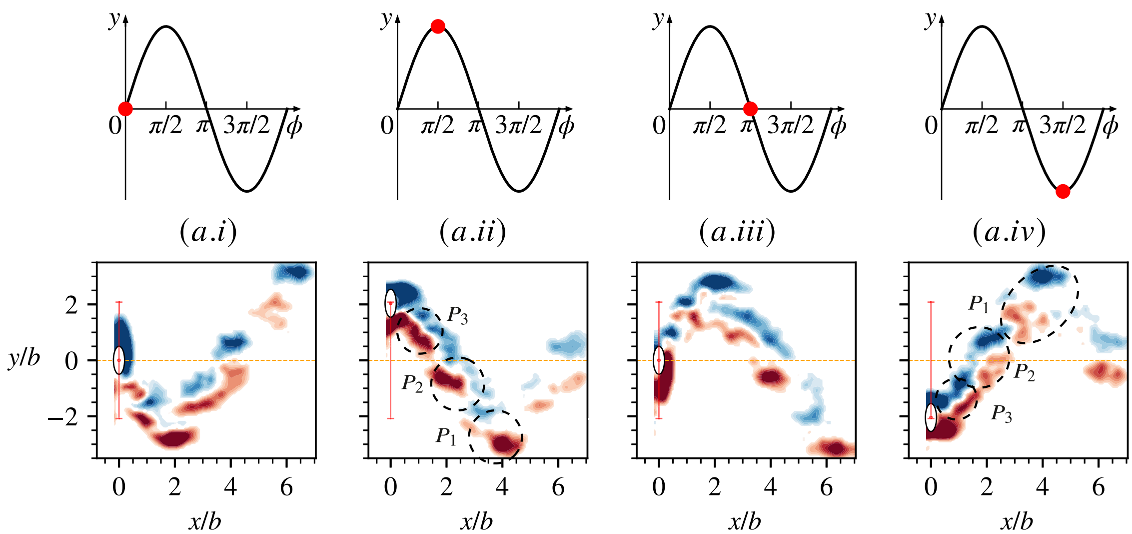

Fig. 13. A 6P pattern is observed in PIV spot measurements for $\epsilon = 2.50$ at $U^* = 11.60$ in V-I regime. The normalized vorticity range is $\omega^* = \omega D/U \in [-3, 3]$.

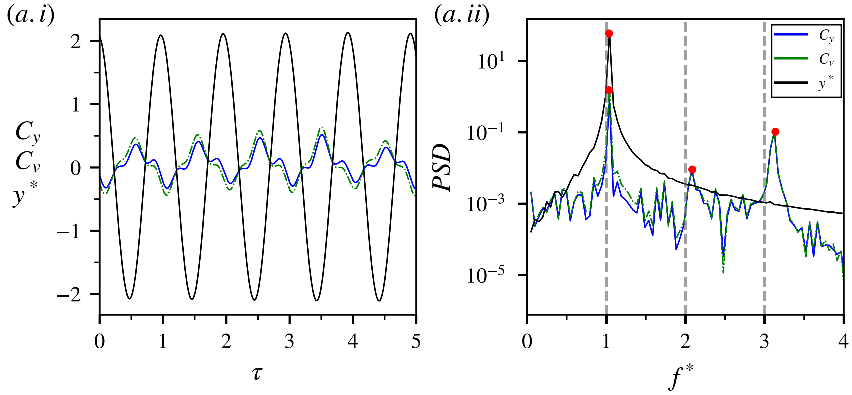

Fig. 14. Sample time traces of the body displacement (y^*), and the coefficients of the total transverse force (C_y) and the vortex force (C_v) for $\epsilon = 2.50$ at $U^* = 11.60$ within the V-I regime, along with the corresponding PSD plots.

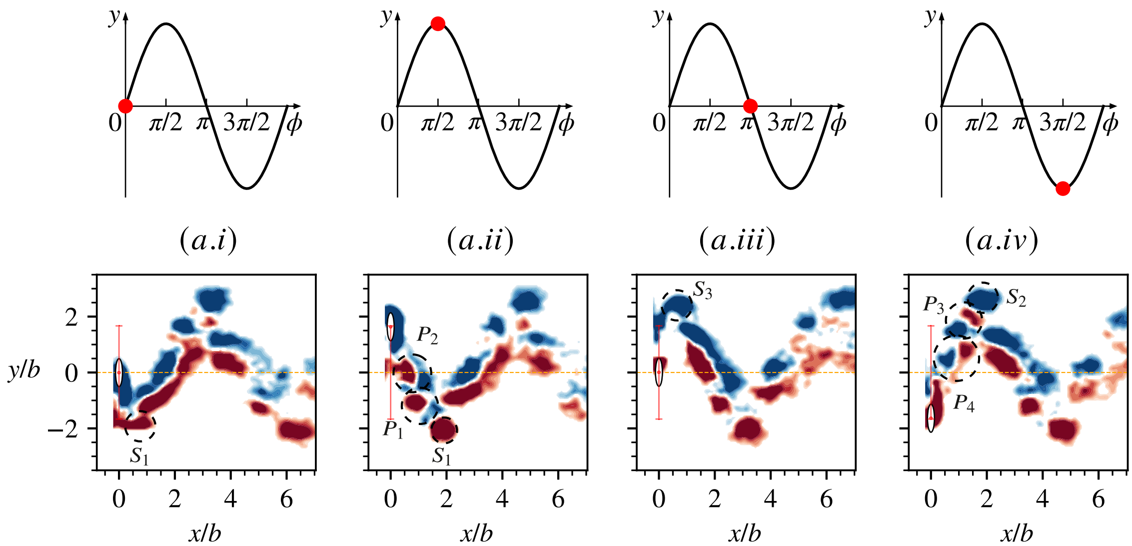

Fig. 15. A 2(2P+S) pattern is observed in PIV spot measurements for $\epsilon = 3.20$ at $U^* = 8.00$ within the V-II regime. The normalized vorticity range is $\omega^* = \omega D/U \in [-3, 3]$.

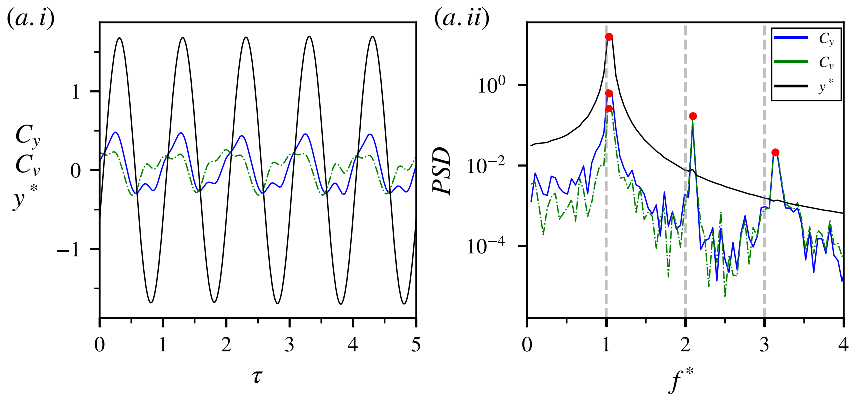

Fig. 16. Sample time traces of the body displacement and the fluid forces (C_y and C_v), together with their frequency power spectra, for $\epsilon = 3.20$ at $U^* = 8.00$ within the V-II regime.

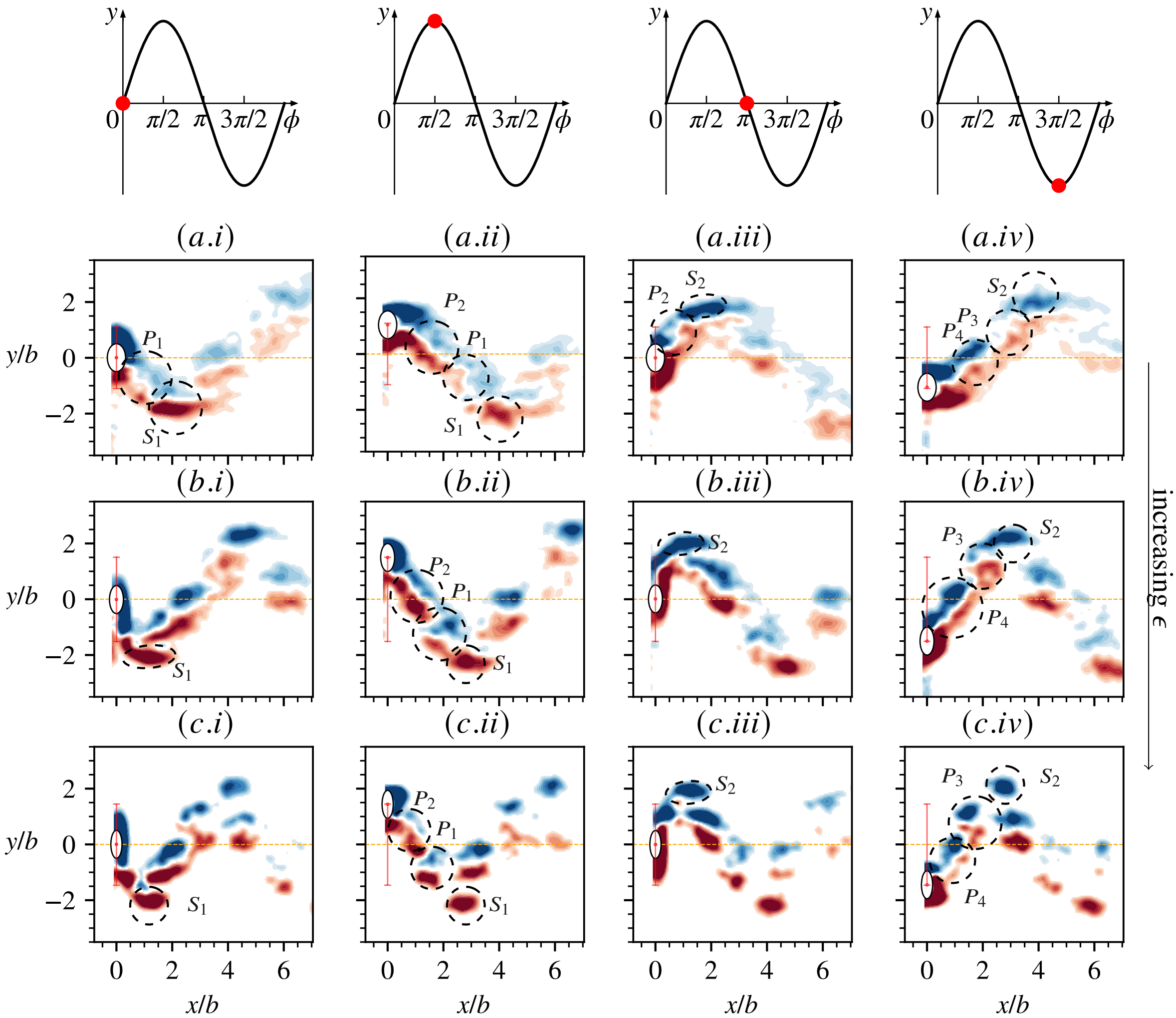

Fig. 17. A 2(2P+S) pattern is observed in PIV spot measurements within the G-I regime for: (*a*) $\epsilon = 1.53$, $U^* = 11.60$, (*b*) $\epsilon = 2.00$, $U^* = 10.00$, (*c*) $\epsilon = 2.50$, $U^* = 8.00$. The normalized vorticity range is $\omega^* = \omega D/U \in [-3, 3]$.

This expression defines the energy conversion of the flow energy passing across the frontal area of an oblate spheroid into extractable energy. The power extraction performance is commonly assessed by its temporal-average power output coefficient over a period of time t (typically over many vibration cycles) (Zhao et al., 2022a):

$$\overline{C}_P = \frac{1}{t}\int_0^t C_P(t)\,dt. \tag{3}$$

Fig. 19 presents the variation of $\overline{C}_p$ as a function of U^* for all ϵ cases tested, where nearly constant mass-damping values $(m^* + C_A)\zeta \approx 0.2634$ are employed (see Table 2). Notably, the maximum $\overline{C}_P$ increases with ϵ from 1.00 to 3.20. Furthermore, as shown in Fig. 20, the case $\epsilon = 3.20$ attains a maximum value of $\overline{C}_P = 0.165$ at $U^* = 6.1$ over the VIV-dominated response. This value represents a significant enhancement of 660%, compared to the maximum value of $\overline{C}_P = 0.025$ observed in the sphere case. It is noteworthy that the potential energy harvesting performance in the G-I mode seems to be more robust than the VIV modes (both Mode I and Mode II) and the V-I mode, as demonstrated by the case of $\epsilon = 2.00$, where the time-averaged power coefficient remains nearly constant at $\overline{C}_P = 0.11$ through its G-I regime, in comparison with case of $\epsilon = 2.50$, where $\overline{C}_P$ decreases gradually with increasing U^* in its V-I regime.

To provide deeper insight into the influence of the mass-damping parameter $(m^* + C_A)\zeta$ on the power extraction performance, Fig. 21 presents variations of the maximum time-averaged power coefficient $\overline{C}_{P_{max}}$ as a function of $(m^* + C_A)\zeta$ for all tested ϵ cases. It should be noted that each $\overline{C}_{P_{max}}$ was obtained from measurements over a range of reduced velocities (e.g., $3 \leqslant U^* \leqslant 12$) for a fixed $(m^* + C_A)\zeta$ value; the value of $(m^* + C_A)\zeta$ was varied by adjusting the structural damping ratio ζ, while the mass ratio m^* was kept constant, with assumed constant C_A in the experiments. This investigation was motivated by the recent study of Han et al.

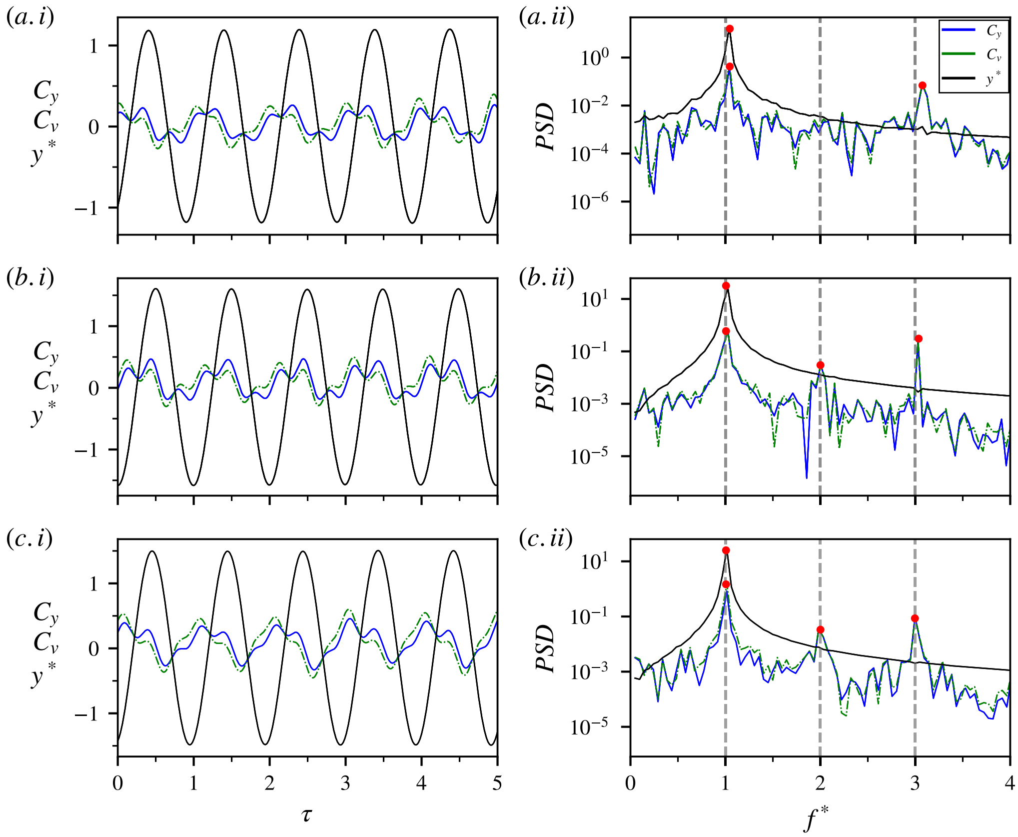

Fig. 18. Sample time traces of the body displacement (y^*), and the coefficients of the total transverse force (C_y) and the vortex force (C_v), together with their PSD plots, for (*a*) $\epsilon = 1.53$ at $U^* = 11.60$, (*b*) $\epsilon = 2.00$ at $U^* = 10.00$, and (*c*) $\epsilon = 2.50$ at $U^* = 8.00$.

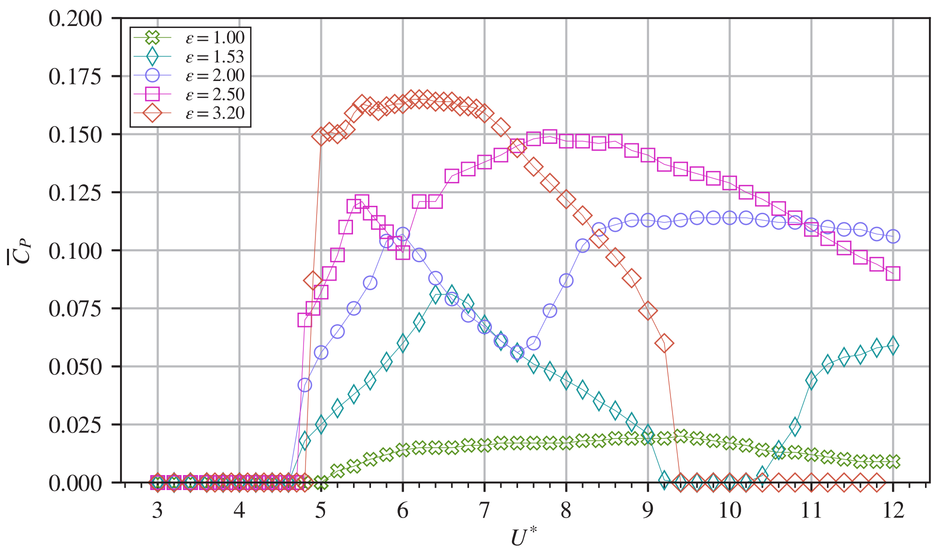

Fig. 19. Variation of the time-averaged power output coefficient $\overline{C}_P$ as a function of U^* for all ϵ cases.

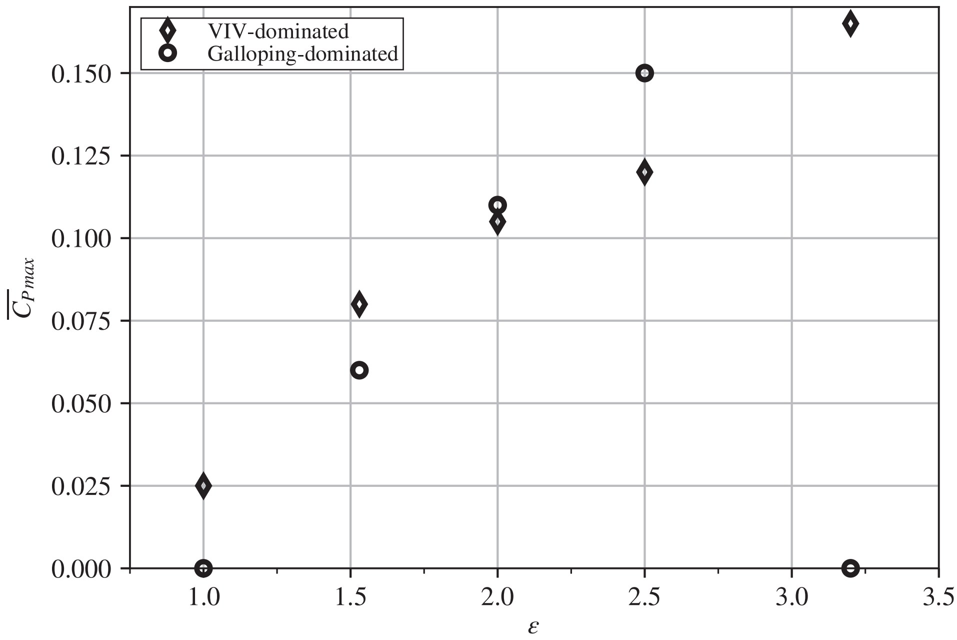

Fig. 20. Variation of the maximum time-averaged power coefficient ($\overline{C}_{P_{max}}$) with ϵ.

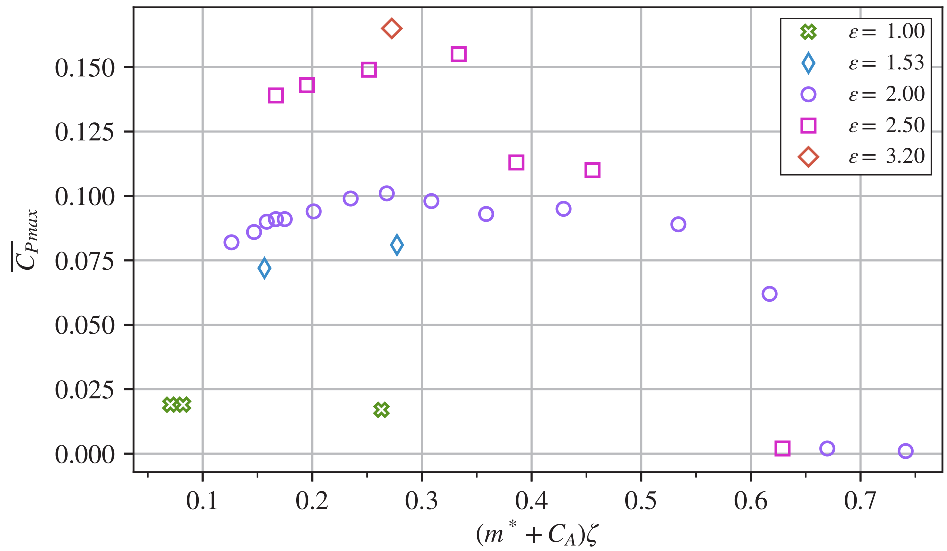

Fig. 21. Variation of the maximum time-averaged power coefficient ($\overline{C}_{P_{max}}$) as a function of $(m^* + C_A)\zeta$ for all ϵ cases.

(2023b) showing that the maximum (time-averaged) power coefficient in VIV of circular cylinders is governed by the mass-damping parameter $(m^* + C_A)\zeta$. It is evident from Fig. 21 that the peak value of $\overline{C}_{P_{max}}$ increases with ϵ, affirming the trends obtained in cases with nearly constant values of $(m^* + C_A)\zeta$, as shown in Fig. 20.

Of particular interest, the cases of ϵ = 2.00 and 2.50 show notable robustness with high-performance $\overline{C}_{P_{max}}$ values remaining stable over the range of $(m^* + C_A)\zeta$ values, i.e., $0.12 < (m^* + C_A)\zeta < 0.52$ for $\epsilon = 2.00$ and $0.15 < (m^* + C_A)\zeta < 0.35$ for $\epsilon = 2.50$. Significantly, in the case of $\epsilon = 2.50$, $\overline{C}_{P_{max}}$ is observed to increase gradually, reaching its peak value of 0.152 at $(m^* + C_A)\zeta = 0.33$, before a sudden reduction at a higher $(m^* + C_A)\zeta$ value. This suggests that similar to VIV of circular cylinders, there may exist an optimal value of $(m^* + C_A)\zeta$ to achieve $\overline{C}_{P_{max}}$ from galloping-dominated responses in spheroids.

For comparison with VIV of a sphere, Table 3 presents the peak $\overline{C}_{P_{max}}$ values from the case of $\epsilon = 3.20$ along with those from a sphere.

Table 3
Comparison of the maximum average power coefficients of an oblate spheroid of $\epsilon = 3.20$ and a sphere.

m^*	C_A	ζ	$(m^* + C_A)\zeta$	$\overline{C}_{P_{max}}$	U^*	Re
Oblate spheroid ($\epsilon = 3.20$)						
39.45	0.337	0.00545	0.2725	0.165	6.1	10 722.39
sphere ($\epsilon = 1.00$)						
12.81	0.590	0.0195	0.2613	0.02	9.4	14 831.371

4. Conclusions

The present study has experimentally investigated FIV responses and implied FIV energy harvesting performance of elastically mounted oblate spheroids with aspect ratios varying from 1.00 to 3.20. The investigations were conducted for spheroids with nearly constant mass-damping $(m^* + C_A)\zeta$ values, which varied in the range of 0.25–0.27 over the reduced velocity range $3.0 \leqslant U^* \leqslant 12.0$, corresponding to Reynolds numbers $4730 \leq Re \leq 20\,120$. Furthermore, the study evaluated the FIV energy harvesting performance of the spheroids as a function of $(m^* + C_A)\zeta$.

The findings showed that the aspect ratio ϵ strongly influences the FIV response of the tested spheroids. For the baseline sphere case, the body vibration is characterized by a pure VIV response, encompassing Mode I over the range of $5.0 \lesssim U^* \lesssim 6.6$, Mode II beyond $U^* > 11$, and a transition region situated in between these two modes. As the sphere is deformed to $\epsilon = 1.53$, following VIV modes – Mode-I and Mode-II – the body vibration becomes desynchronized over the range of $9.2 \leqslant U^* \leqslant 10.2$, before recovering into a galloping-dominated mode, denoted by G-I, for $U^* > 10.2$. With further body deformation to $\epsilon = 2.00$, the body vibration predominantly exhibits three significant regimes: Mode I, Mode II, and G-I, with smooth transitions observed between them. As ϵ is increased to 2.5, in addition to the three significant regimes observed in the case of $\epsilon = 2.00$, a new regime associated with a VIV-Galloping response mode, denoted by V-I, is encountered for $U^* > 10.0$. Notably, in comparison to G-I mode, V-I mode displays a much weaker second harmonic ($f^* \simeq 2$) in both $f^*_{C_y}$ and $f^*_{C_v}$, and a lower growth rate of A^*_{10} with U^*. The maximum vibration amplitude of all tested ϵ cases is observed to be $A^*_{10} = 2.17$ at $U^* = 12.0$ in the V-I mode response of $\epsilon = 2.50$. With the most significant body formation in the present study, $\epsilon = 3.20$, the spheroid surprisingly exhibits a large-amplitude vibration response with Mode-I vortex shedding over the range $4.9 \leqslant U^* \leqslant 7.0$, before transitioning to a VIV-dominated regime V-II between $7 \leqslant U^* \leqslant 9$. The maximum amplitude in this V-II regime observed is $A^*_{10} = 1.70$, an increase of 143% compared to the peak A^*_{10} value observed in Mode-II for $\epsilon = 1.53$.

Furthermore, planar PIV measurements have unveiled significant changes in the wake structure as ϵ increased from the sphere case. It has been observed that during the galloping-dominated regime, a greater number of coherent vortical structures were shed per oscillation cycle compared to the VIV-dominated regimes. This observation is correlated with high-order harmonic frequency components in the fluid forces, similar to the phenomena observed in previous studies of D-section or square cylinders undergoing galloping oscillations.

The investigation of the FIV energy harvesting performance of the tested spheroids showed that the peak power output coefficient tends to increase with ϵ. The evaluations revealed a maximum time-averaged power coefficient of $\overline{C}_{P_{max}} = 0.165$ was achieved in the M-I mode response of $\epsilon = 3.20$. This value was approximately 660% higher than that observed in VIV of spheres. This suggests that FIV energy harvesting from galloping-dominated responses of oblate spheroids holds significant practical potential. Additionally, the study of $\overline{C}_{P_{max}}$ with varying mass-damping $(m^* + C_A)\zeta$ values suggests that, similar to VIV of circular cylinders, there may exist an optimal value of $(m^* + C_A)\zeta$ to achieve $\overline{C}_{P_{max}}$ from galloping-dominated responses in spheroids.

The findings highlight the distinctive nature of FIV responses in 3D oblate spheroids compared to 2D bluff bodies like elliptical, D-section, and square cylinders. Therefore, performing a quasi-steady instability analysis is recommended to gain deeper insights into the underlying mechanisms governing the FIV responses of 3D oblate spheroids. Additionally, further research to comprehensively understand the 3D flow structures associated with various response modes in FIV of 3D oblate spheroids would be of great interest. In closing, note that additional experiments for $\epsilon = 3.20$ indicated some sensitivity (not shown in the present study) in ranges of $4.6 \lesssim U^* < 6$ and $7.8 \lesssim U^* < 9.6$, near two transitions in the amplitude response. Therefore, further investigations are warranted to assess the sensitivity of the FIV responses of the spheroids, particularly for high ϵ, under various experimental conditions, including initial flow conditions (to investigate hysteresis effects), Reynolds number, mass ratio, and damping ratio.

CRediT authorship contribution statement

Adrian Cordero Obando: Conceptualization, Formal analysis, Investigation, Methodology, Project administration, Visualization, Writing – original draft, Data curation, Writing – review & editing. **Mark C. Thompson:** Supervision, Validation, Writing – review & editing, Resources, Formal analysis. **Kerry Hourigan:** Supervision, Validation, Writing – review & editing, Formal analysis, Funding acquisition, Resources. **Jisheng Zhao:** Formal analysis, Funding acquisition, Resources, Supervision, Validation, Writing – review & editing.

Declaration of competing interest

The authors declare that they have no known competing financial interests or personal relationships that could have appeared to influence the work reported in this paper.

Data availability

Data will be made available on request.

Acknowledgments

This work was supported by the Australian Research Council (Discovery Early Career Researcher Award DE200101650 and Discovery Project grant DP210100990). The authors would also like to acknowledge the Monash Energy Institute for providing a travel grant to support A.C. in attending the ERCOFTAC 2023 Symposium.

References

Bearman, P.W., 1984. Vortex shedding from oscillating bluff bodies. Annu. Rev. Fluid Mech. 16 (1), 195–222.
Bearman, P.W., 2011. Circular cylinder wakes and vortex-induced vibrations. J. Fluids Struct. 27 (5), 648–658.
Bearman, P., Currie, I., 1979. Pressure-fluctuation measurements on an oscillating circular cylinder. J. Fluid Mech. 91 (4), 661–677.
Bearman, P.W., Gartshore, I.S., Maull, D., Parkinson, G.V., 1987. Experiments on flow-induced vibration of a square-section cylinder. J. Fluids Struct. 1 (1), 19–34.
Bernitsas, M.M., Raghavan, K., Ben-Simons, Y., Garcia, E.H.M., 2008. Vortex induced vibration aquatic clean energy: A new concept in generation of clean and renewable energy from fluid flow. J. Offshore Mech. Arct. Eng. 130, 041101.
Bishop, R.E.D., Hassan, A., 1964. The lift and drag forces on a circular cylinder oscillating in a flowing fluid. Proc. R. Soc. Lond. A 277 (1368), 51–75.
Blevins, R.D., 1990. Flow-Induced Vibration, second ed. Krieger Publishing Company, Malabar, p. 377.
Brooks, P.H.N., 1960. Experimental Investigation of the Aeroelastic Instability of Bluff Two-Dimensional Cylinders. M.A.Sc., University of British Columbia.
den Hartog, J.P., 1932. Transmission line vibration due to sleet. Trans. Am. Inst. Electr. Eng. 51 (4), 1074–1076.
Feng, C.C., 1968. The Measurement of Vortex Induced Effects in Flow Past Stationary and Oscillating Circular and D-Section Cylinders (Ph.D. thesis). (October), The University of British Columbia.
Fouras, A., Lo Jacono, D., Hourigan, K., 2008. Target-free stereo PIV: a novel technique with inherent error estimation and improved accuracy. Exp. Fluids 44 (2), 317–329.
Franzini, G.R., Fujarra, A.L.C., Meneghini, J.R., Korkischko, I., Franciss, R., 2009. Experimental investigation of vortex-induced vibration on rigid, smooth and inclined cylinders. J. Fluids Struct. 25 (4), 742–750.
Gabbai, R.D., Benaroya, H., 2005. An overview of modeling and experiments of vortex-induced vibration of circular cylinders. J. Sound Vib. 282 (3–5), 575–616.
Govardhan, R.N., Williamson, C.H.K., 2000. Modes of vortex formation and frequency response of a freely vibrating cylinder. J. Fluid Mech. 420, 85–130.
Govardhan, R.N., Williamson, C.H.K., 2005. Vortex-induced vibrations of a sphere. J. Fluid Mech. 531, 11–47.
Gu, W., Chyu, C., Rockwell, D., 1994. Timing of vortex formation from an oscillating cylinder. Phys. Fluids 6 (11), 3677–3682.
Hahn, S.L., 1996. Hilbert Transforms in Signal Processing. Artech House Boston.
Han, P., de Langre, E., Thompson, M.C., Hourigan, K., Zhao, J., 2023a. Vortex-induced vibration forever even with high structural damping. J. Fluid Mech. 962, A13.
Han, P., Huang, Q., Pan, G., Qin, D., Wang, W., Gonçalves, R.T., Zhao, J., 2023b. Optimal energy harvesting efficiency from vortex-induced vibration of a circular cylinder. Ocean Eng. 282, 114869.
Jauvtis, N., Govardhan, R.N., Williamson, C.H.K., 2001. Multilple modes of vortex-induced vibration of a sphere. J. Fluids Struct. 15 (3–4), 555–563.
Khalak, A., Williamson, C.H.K., 1996. Dynamics of a hydroelastic cylinder with very low mass and damping. J. Fluids Struct. 10 (5), 455–472.
Khalak, A., Williamson, C.H.K., 1999. Motions, forces and mode transitions in vortex-induced vibrations at low mass-damping. J. Fluids Struct. 13 (7–8), 813–851.
Leontini, J.S., Griffith, M., Lo Jacono, D., Sheridan, J., 2018. The flow-induced vibration of an elliptical cross-section at varying angles of attack. J. Fluids Struct. 78, 356–373.
Lighthill, J., 1986. Fundamentals concerning wave loading on offshore structures. J. Fluid Mech. 173, 667–681.
Lo, J.C.C., Thompson, M.C., Hourigan, K., Zhao, J., 2023. The effect of structural damping on flow-induced vibration of a thin elliptical cylinder. J. Fluid Mech. Accepted.
McQueen, T., Zhao, J., Sheridan, J., Thompson, M.C., 2020. Feedback control of flow-induced vibration of a sphere. J. Fluid Mech. 889, A30.
Naudascher, E., Rockwell, D., 2005. Flow-Induced Vibrations: An Engineering Guide. Dover Publications.
Navros, Yogeswaran, V., Sen, S., Mittal, S., 2014. Free vibrations of an elliptic cylinder at low Reynolds numbers. J. Fluids Struct. 51, 55–67.
Nemes, A., Zhao, J., Lo Jacono, D., Sheridan, J., 2012. The interaction between flow-induced vibration mechanisms of a square cylinder with varying angles of attack. J. Fluid Mech. 710, 102–130.
Païdoussis, M., Price, S., de Langre, E., 2010. Fluid-Structure Interactions: Cross-Flow-Induced Instabilities. Cambridge University Press.
Rajamuni, M.M., Hourigan, K., Thompson, M.C., 2021. Vortex-induced vibration of a sphere close to or piercing a free surface. J. Fluid Mech. 929, A41.
Sareen, A., Zhao, J., Lo Jacono, D., Sheridan, J., Hourigan, K., Thompson, M.C., 2018a. Vortex-induced vibration of a rotating sphere. J. Fluid Mech. 837, 258–292.
Sareen, A., Zhao, J., Sheridan, J., Hourigan, K., Thompson, M.C., 2018b. Vortex-induced vibrations of a sphere close to a free surface. J. Fluid Mech. 846, 1023–1058.
Sarpkaya, T., 2004. A critical review of the intrinsic nature of vortex-induced vibrations. J. Fluids Struct. 19 (4), 389–447.
Soti, A.K., Zhao, J., Thompson, M.C., Sheridan, J., Bhardwaj, R., 2018. Damping effects on vortex-induced vibration of a circular cylinder and implications for power extraction. J. Fluids Struct. 81, 289–308.
Williamson, C.H.K., Govardhan, R.N., 2004. Vortex-induced vibration. Annu. Rev. Fluid Mech. 36, 413–455.
Williamson, C.H.K., Roshko, A., 1988. Vortex formation in the wake of an oscillating cylinder. J. Fluids Struct. 2 (4), 355–381.
Zhao, J., Hourigan, K., Thompson, M.C., 2018a. Flow-induced vibration of D-section cylinders: an afterbody is not essential for vortex induced vibration. J. Fluid Mech. 851, 317–343.
Zhao, J., Hourigan, K., Thompson, M.C., 2019. Dynamic response of elliptical cylinders undergoing transverse flow-induced vibration. J. Fluids Struct. 89, 123–131.
Zhao, J., Leontini, J.S., Lo Jacono, D., Sheridan, J., 2014. Fluid–structure interaction of a square cylinder at different angles of attack. J. Fluid Mech. 747, 688–721.
Zhao, J., Lo Jacono, D., Sheridan, J., Hourigan, K., Thompson, M.C., 2018b. Experimental investigation of in-line flow-induced vibration of a rotating cylinder. J. Fluid Mech. 847, 664–699.
Zhao, J., Nemes, A., Lo Jacono, D., Sheridan, J., 2018c. Branch/mode competition in the flow-induced vibration of a square cylinder. Philos. Trans. R. Soc. Lond. Ser. A 376, 20170243.
Zhao, J., Thompson, M.C., Hourigan, K., 2022a. Damping effect on transverse flow-induced vibration of a rotating circular cylinder and its implied energy harvesting performance. Phys. Rev. Fluids 7 (2), 023905.
Zhao, J., Thompson, M.C., Hourigan, K., 2022b. Decomposition of fluid forcing and phase synchronisation for in-line vortex-induced vibration of a circular cylinder. J. Fluid Mech. 941, R4.